

Understanding Aerosol-Cloud Interactions ~~Using~~Using a Single-Column Model: ~~Intercomparison with Process Level Models and Evaluation against~~ for a Cold-Air Outbreak Case during the ACTIVATE Campaign~~Field Measurements Campaign~~

Shuaiqi Tang^{1,2}, Hailong Wang¹, Xiang-Yu Li¹, Jingyi Chen^{1,3}, Armin Sorooshian^{4,5,2,3}, Xubin Zeng⁴~~Zeng~~^{4,2}, Ewan Crosbie^{6,7,4,5}, Kenneth L. ~~Thornhill~~⁶~~Thornhill~~^{6,4}, Luke D. ~~Ziemba~~⁶~~Ziemba~~^{6,4}, Christiane ~~Voigt~~⁸~~Voigt~~^{6,7,8,9}

¹Atmospheric, Climate, and Earth Sciences Division, Pacific Northwest National Laboratory, Richland, WA, USA

²[School of Atmospheric Sciences, Nanjing University, Nanjing, China](#)

³[School of Atmospheric Physics, Nanjing University of Information Science and Technology, Nanjing, China](#)

⁴~~Department~~^{4,2}~~Department~~ of Hydrology and Atmospheric Sciences, The University of Arizona, Tucson, AZ, USA

⁵~~Department~~^{5,3}~~Department~~ of Chemical and Environmental Engineering, The University of Arizona, Tucson, AZ, USA

⁶~~NASA~~^{6,4}~~NASA~~ Langley Research Center, Hampton, VA, USA

⁷~~Analytical~~^{7,5}~~Analytical~~ Mechanics Associates Inc., Hampton, VA, USA

⁸~~Deutsches~~^{8,6}~~Deutsches~~ Zentrum für Luft- und Raumfahrt, Oberpfaffenhofen, Germany

⁹~~Johannes~~^{9,7}~~Johannes~~ Gutenberg-Universität, Mainz, Germany

Correspondence to: Shuaiqi Tang (shuaiqi.tang@nju.edu.cn) and Hailong Wang (hailong.wang@pnnl.gov)

Abstract. Marine boundary-layer clouds play a critical role in ~~the~~ Earth's energy balance. Their microphysical and radiative properties are highly impacted by ambient aerosols and ~~dynamic~~~~dynamical~~ forcings. In this study, we evaluate the representation of these clouds and related aerosol-cloud ~~interaction~~~~interactions~~ processes in the single-column version of ~~the~~ E3SM climate model (SCM), against field measurements collected during the NASA ACTIVATE campaign over the western North Atlantic, as well as intercompare ~~data~~~~results~~ with high-resolution process-level models. ~~Results-~~~~We~~ show that E3SM-SCM, ~~driven by the ERA5 reanalysis,~~ ~~well~~ reproduces ~~well~~ the ~~macrophysical~~ ~~properties~~~~properties~~ of post-frontal boundary layer clouds ~~infer~~~~in~~ a cold-air outbreak (CAO) case. However, it generates fewer but ~~bigger~~~~larger~~ cloud droplets, ~~compared to aircraft measurements. Further sensitivity tests show that~~ ~~the~~~~both~~~~the~~ underestimation of ~~both~~ aerosol number concentration and ~~weaker~~ vertical velocity variance contributes to this bias. ~~cloud properties as good as the high resolution WRF simulations. For stronger surface forcings combined with a weaker subsidence taken from a WRF cloud resolving simulation, both E3SM-SCM and WRF large eddy simulation produce thicker clouds. This indicates that a proper combination of large scale dynamics, sub-grid scale parameterizations, and model configurations is needed to obtain optimal performance of cloud simulations. In the E3SM-SCM sensitivity tests with fixed dynamics but perturbed aerosol properties, higher aerosol number concentration~~ Aerosol-cloud interactions are examined by perturbing prescribed aerosol properties in E3SM-SCM, with fixed dynamics. Higher aerosol number concentration or hygroscopicity leads to more numerous but smaller cloud droplets, resulting in a stronger ~~cooling in terms of~~~~via~~ shortwave cloud forcing. ~~(i.e., stronger radiative~~

34 ~~cooling~~). This apparent Twomey effect is consistent with prior climate model studies. Cloud liquid water path shows a
35 weakly positive relation with cloud droplet number concentration ~~associated with adue to precipitation suppression effect,~~
36 ~~which is different from the nonlinear relation approximated from prior observations and E3SM studies. This weak aerosol~~
37 ~~effect on the cloud macrophysics may be attributed to the dominant impact masking of strong dynamical forcing~~
38 ~~associated with the CAO. CAO warranting future investigation.~~ Our findings indicate that the SCM framework is a key tool to
39 bridge the gap between climate models, ~~high-resolution process-level~~ models, and field observations to facilitate process-
40 level understanding.

41 **1 Introduction**

42 Marine boundary layer (MBL) clouds are the dominant cloud type over oceans, with an annual mean occurrence frequency
43 of 45% (Warren et al., 1988) and coverage of 34% including stratocumulus, stratus, and fog (Warren et al., 1988) or 23% for
44 stratocumulus only (Wood, 2012). Its high reflectivity ~~overlapped in contrast~~ with ~~the~~ low-reflective ocean surface
45 underneath leads to a strong shortwave cooling effect, but its longwave warming effect is neglectable due to low cloud top
46 height (Hartmann et al., 1992). In global climate models (GCM), the representation of MBL clouds and their radiative effects
47 has long been a challenging task (e.g., Bony and Dufresne, 2005; Brunke et al., 2019). Even the latest Coupled Model
48 Intercomparison Project Phase 6 (CMIP6) models still have a large inter-model spread in the cloud shortwave effect (Bock et
49 al., 2020) that introduces large uncertainties to climate projection.

50
51 The western North Atlantic Ocean (WNAO) is one of the regions dominated by MBL clouds. The Gulf Stream with ~~a~~ large
52 spatial gradient in sea surface temperature (SST), strong synoptical systems such as tropical and extratropical cyclones, ~~and~~
53 aerosols generated locally or transported from the adjacent North American continent, all contribute to the complex aerosol-
54 cloud-meteorology-ocean interactions over this region (e.g., Painemal et al., 2021; Corral et al., 2021). Recently, Sorooshian
55 et al. (2020) provided an overview of the past atmospheric studies over ~~the~~ WNAO region, followed by more detailed
56 ~~overviews analysis on of atmospheric circulation, boundary layer features, and clouds, and precipitation~~ (Painemal et al.,
57 2021), ~~clouds and precipitation~~ (Kirschler et al., 2023), and atmospheric chemistry and aerosols (Corral et al., 2021).
58 However, among 715 peer-reviewed publications between 1946 and 2019, only 2% of the studies are related to aerosol-cloud
59 interactions (ACI) (Sorooshian et al., 2020). This indicates that ACI over ~~the~~ WNAO region is underexplored, ~~considering~~
60 ~~that~~ ~~which is a critical knowledge gap to start filling as~~ ACI has long been emphasized as the largest uncertainty source in
61 climate model simulations (IPCC, 2013, 2021).

62
63 With ~~the~~ limited prior understanding, ~~a three year field campaign, the~~ Aerosol Cloud meTeorology Interactions oVer the
64 western ATlantic Experiment (ACTIVATE) ~~project~~ (Sorooshian et al., 2019), was conducted between 2020 and 2022
65 targeting the complex ACI for MBL clouds over the WNAO region. Two aircraft flew simultaneously in spatial coordination:

66 a low-flying aircraft ~~making~~ conducted in-situ measurements and a high-flying aircraft ~~making~~ de remote-sensing
67 measurements and ~~releasing~~ released dropsondes. Among the ~~total of 162~~ total joint flights, 12 of them were conducted as
68 “process study” flights (Sorooshian et al., 2023), during which the ~~flying-flight~~ patterns of the two flights were carefully
69 designed to provide detailed information about the scene encompassing the clouds of interest. In some cases, including the
70 case chosen for this study, the high-flying aircraft released numerous dropsondes along a large circle and the low-flying
71 aircraft conducted stacked below-, in-, and above-cloud flight legs within the circle. The dropsonde-derived divergence
72 profiles and surface fluxes have been used to constrain process-level ~~modeling~~ modeling studies (Chen et al., 2022; Li et al.,
73 2022; Li et al., 2023).

74
75 A few process-level studies have been conducted using the Weather Research and Forecasting (WRF) model nested domain
76 regional simulation (Chen et al., 2022) and WRF large-eddy simulation (LES) (Li et al., 2022; Li et al., 2023). The WRF
77 regional simulation has an inner domain at 1 km convection-permitting horizontal grid spacing, hereafter referred to as
78 cloud-resolving model (CRM) simulation in this study. Note that this is different from the conventionally defined CRM,
79 which is usually run with prescribed large-scale forcing, and periodic boundary conditions, in a limited region analogous to
80 a single-column model (SCM) (Randall et al., 1996). A post-frontal MBL cloud case related to a winter cold-air outbreak
81 (CAO) was studied in these CRM and LES studies. Chen et al. (2022) successfully simulated the observed cloud roll
82 structure in WRF-CRM. They found that a distinctive boundary layer wind direction shear favours the formation and
83 persistence of cloud rolls. Li et al. (2022) validated the ERA5-derived large-scale forcing with dropsonde-derived forcing
84 and tested the sensitivity of WRF-LES to the large-scale forcing. They furthermore investigated ACI with a series of LES
85 sensitivity experiments based on spatial variability in aircraft-measured aerosol and cloud properties (Li et al., 2023).

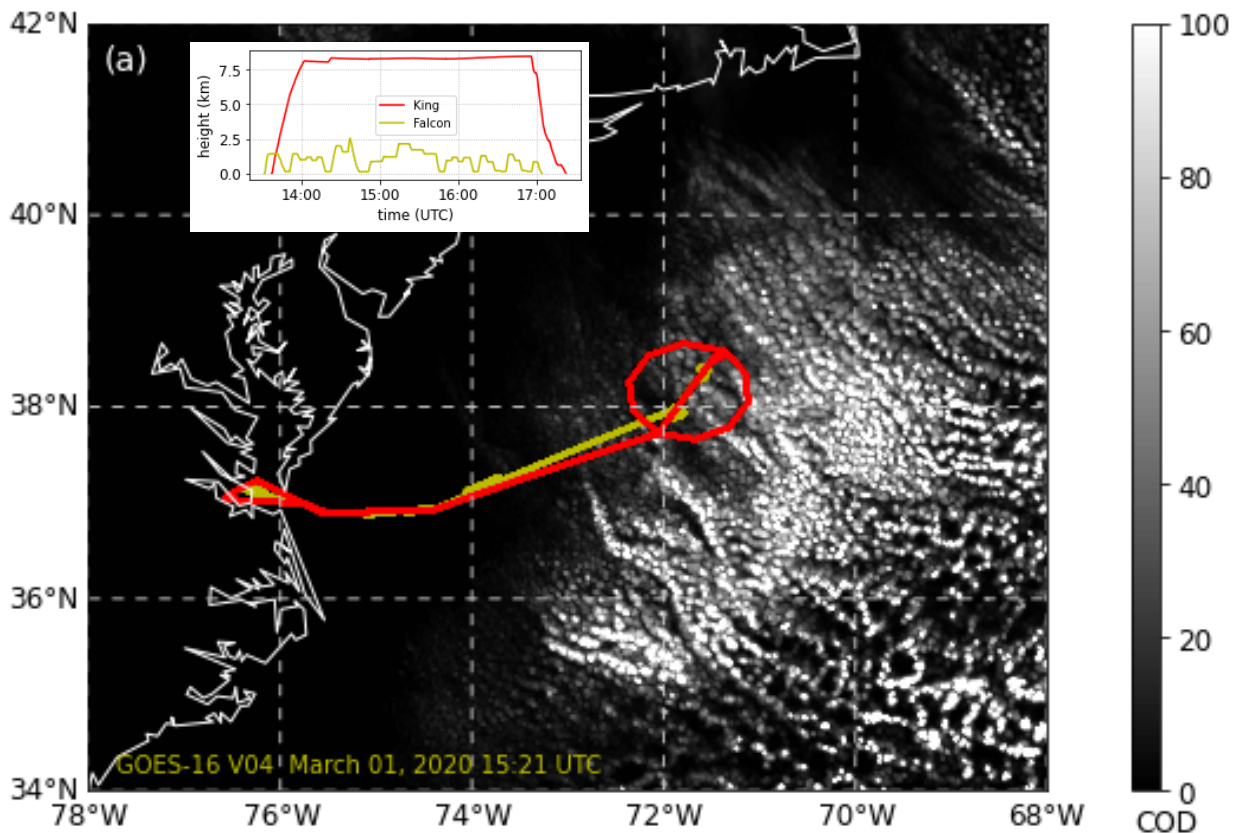
86
87 In this study, we focus on SCM simulations for the same CAO case as that being investigated in the CRM/LES
88 studies (Chen et al., 2022; Li et al., 2022; Li et al., 2023). We tried a few other CAO cases observed during the
89 ACTIVATE campaign, but the SCM cannot produce the observed boundary-layer structure and cloud evolution in those
90 cases, likely due to weaker CAO forcings and not as well-defined large-scale boundary conditions for the SCM. It is critical
91 to have well-simulated clouds for the aerosol-cloud interaction sensitivity tests. Therefore, our study is limited to this single
92 case. With simulations from As these all the above models simulate the same case in different complexity and resolution, we
93 are now able to make a detailed process-level analysis of ACI through the multi-scale LES-CRM-SCM intercomparison.
94 This is a step further than studies using individual models. Our first goal is to understand how the CAO-related post-frontal
95 MBL clouds are simulated in the SCM in contrast to observations and the LES and CRM simulations, and the observations.
96 Another goal is to explore how the simulated MBL clouds respond to perturbations of aerosol properties prescribed into the
97 SCM through sensitivity studies and how the ACI metrics relations metrics or cloud susceptibility holds susceptibility
98 perform hold under the CAO condition observed during the ACTIVATE campaign, using observations collected during the
99 ACTIVATE campaign. We introduce the selected case, data, and models in Sect. 2, show the general SCM

100 ~~performance performances and intercomparison intercompare~~ SCM with CRM and LES results in Sect. 3, ~~explore and then~~
101 ~~show results of~~ explore the cloud responses to aerosol perturbations through SCM sensitivity studies in Sect. 4, ~~and then~~
102 ~~further investigate LWP susceptibility in Sect. 5~~. Conclusion remarks are provided in Sect. ~~6~~56.

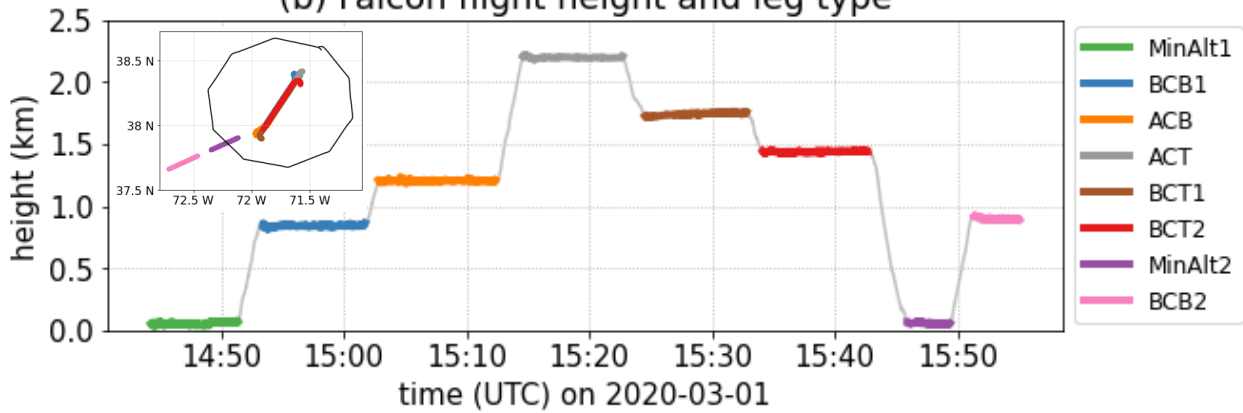
103 **2 Case Description, Observations, and Simulations**

104 **2.1 The CAO case on 1 March 2020**

105 This study focuses on a CAO case observed on 1 March 2020, after the passage of a cold front. A large area of MBL clouds
106 formed associated with warm SST, cold air advection, and large-scale subsidence. The ACTIVATE campaign deployed two
107 spatially coordinated aircraft to measure the post-frontal MBL clouds from different heights (Fig. 1a). The High Spectral
108 Resolution Lidar – generation 2 (HSRL-2) from the high-flying King Air aircraft measured vertical aerosol backscattering
109 profiles, which were used to estimate the cloud top height. The King Air also released 11 dropsondes in a ~110 km diameter
110 circle centered near (38.1°N, 71.7°W) to measure the vertical profiles of the meteorology state. The low-flying Falcon
111 aircraft mainly provided in-situ trace gas, aerosol, and cloud microphysical measurements. The entire Falcon flight is divided
112 into many flight “legs” (Dadashazar et al., 2022b). Each flight leg represents a segment during which the flight is measuring
113 under a specific condition at constant altitude (e.g., below/in/above cloud) or is in a specific operation mode (e.g., ascending,
114 descending). For most of this study, we focus on eight flight legs within or near the dropsonde array domain (Fig. 1b),
115 including two minimum-altitude (MinAlt) legs, two below-cloud-base (BCB) legs, one above-cloud-base (ACB) leg, two
116 below-cloud-top (BCT) legs, and one above-cloud-top (ACT) leg. The first six flight legs were stacked ~~at~~ different heights
117 as a “wall” pattern. The last two legs were ~~flying~~ flown outside the dropsonde domain but ~~were~~ were used here for
118 sensitivity study purposes.



(b) Falcon flight height and leg type



119

120 **Figure 1: (a).** ACTIVATE flight tracks for Falcon (yellow) and King Air (red) aircraft on 1 March 2020 (RF13), overlaid with
 121 GOES-16 satellite-measured cloud optical depth (COD) at 15:21 UTC. The insert shows the time series of flight altitude for both
 122 aircraft. (b) Time and height of the eight Falcon flight legs within or near the dropsonde array domain. The insert is the horizontal
 123 location of the eight flight legs and the dropsonde domain (thin black line). Acronym of flight leg types: BCB: below cloud base;
 124 ACB: above cloud base; ACT: above cloud top; BCT: below cloud top; MinAlt: minimum altitude (~120-150 m above ground level
 125 (AGL)).

126 2.2 Forcing and Evaluation Data

127 Table 1 lists the aircraft measurements used in this study. These observational data are used mainly for two purposes: driving
 128 models as initial and boundary conditions and evaluating model results. Satellite measurements and reanalysis data are also
 129 used to supplement the aircraft measurements to give a more complete view and fill data gaps when aircraft data are
 130 unavailable. Specifically, the liquid water path (LWP) and the ice water path (IWP) are retrieved from GOES-16
 131 geostationary satellite using the Visible Infrared Solar-Infrared Split Window Technique (VISST) (Minnis et al., 2008;
 132 Minnis et al., 2011) algorithm from the NASA-Langley Satellite Cloud Observations and Radiative Property retrieval
 133 System (SatCORPS). ERA5 reanalysis [data](#) (Hersbach et al., 2020) [isare](#) used to provide model initial and boundary
 134 conditions to drive the WRF-CRM simulation, and to supplement the large-scale forcing used by WRF-LES and E3SM-
 135 SCM. More details of the large-scale forcing are given in the next subsection.

136

137 **Table 1: Aircraft measurements used in this study.**

Instrument	Measurements	Platform	Data Version
GPS	Flight location (lat, lon, alt)	Falcon	R4
N/A	Flight leg flag	Falcon	R3
Five-port pressure system (TAMMS)	3-D winds	Falcon	R4
Rosemount 102 sensor	Temperature	Falcon	R4
Diode laser hygrometer (DLH)	Water vapor mixing ratio	Falcon	R1
Scanning Mobility Particle Sizer (SMPS)	Aerosol number size distribution (2.97 – 94.0 nm)	Falcon	R4
Laser Aerosol Spectrometer (LAS)	Aerosol number size distribution (93.9 – 3487.5 nm)	Falcon	R3
High-Resolution Time-of-Flight Aerosol Mass Spectrometer (AMS)	Mass concentration of aerosol composition (Organic, Sulphate, Nitrate, Ammonium, Chloride)	Falcon	R2
Cloud Condensation Nuclei (CCN) Counter	CCN number concentration with supersaturation (SS) scanning from ~ 0.16% to 0.72%	Falcon	R0
Fast Cloud Droplet Probe (FCDP)	Cloud droplet number size distribution (3 – 50 μm), liquid water content (LWC), droplet number concentration, and effective radius	Falcon	R1
GPS	Flight location (lat, lon, alt)	King Air	R0
High Spectral Resolution Lidar (HSRL-2)	Cloud top height	King Air	R0
Dropsonde (Vömel et al., 2023)	Temperature, pressure, altitude, relative humidity, U wind, V wind	King Air	R1

138 2.3 Model Simulations

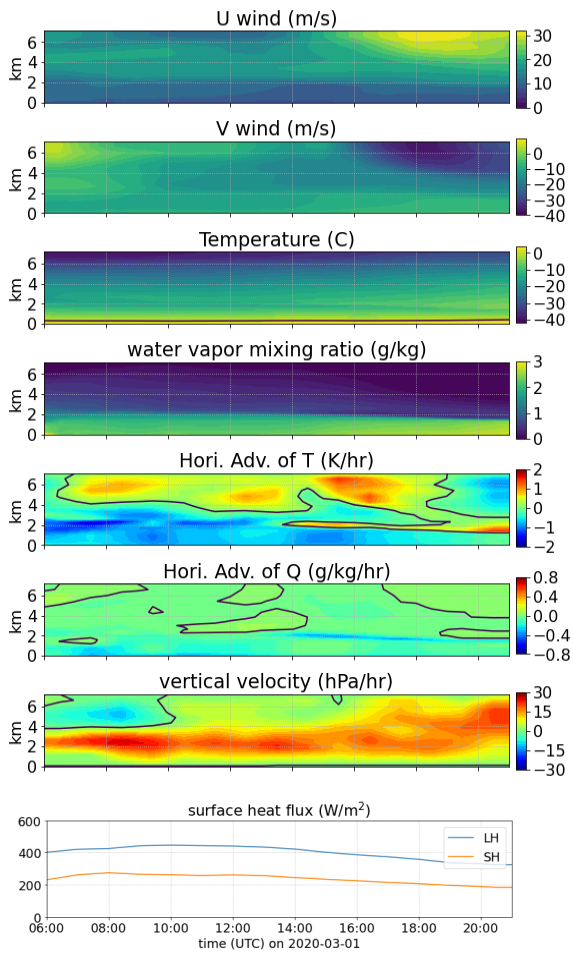
139 The SCM used in this study is based on the Energy Exascale Earth System Model (E3SM) version 2 (Golaz et al., 2022;
 140 Bogenschutz et al., 2020). It includes a deep convective parameterization from Zhang and McFarlane (1995) with [the](#)

141 modification in convective trigger from Xie et al. (2019) to improve the diurnal cycle of precipitation, a two-moment
142 microphysics scheme from Gettelman and Morrison (2015) (MG2), and a Cloud Layers Unified By Binormals (CLUBB)
143 (Golaz et al., 2002; Larson and Golaz, 2005) parameterization for turbulence, shallow convection and macrophysics all-
144 together. Some parameters of these schemes were systematically re-tuned to improve the overall performance of subtropical
145 stratocumulus clouds (Ma et al., 2022). Aerosols generally require a long spin-up time that is unrealistic during the relatively
146 short SCM case durations. Instead of directly using the aerosol scheme, three options ~~has~~ have been implemented in
147 E3SM-SCM to treat aerosols: specifying droplet and ice number concentrations to “bypass” ACI, using “prescribed”
148 aerosols from a 10-year E3SM climatology simulation under present-day forcing conditions, or using “observed” aerosol
149 information if available (Bogenschutz et al., 2020). The information of three lognormal distribution modes of aerosols
150 (Aitken, accumulation, and coarse) is needed in the “prescribed” and “observed” methods to replace the output from the
151 aerosol scheme, which is a 3-mode Modal Aerosol Module (MAM3) (Liu et al., 2012) in the E3SM SCM configuration.
152 Note that this differs from the default MAM4 scheme (Liu et al., 2016) in E3SM GCM. The “observed” method currently
153 does not include vertical variation of aerosols (i.e., observed aerosol information is applied to all vertical layers from the
154 surface to the model top). Therefore, to investigate ACI and the impact of aerosol vertical distribution on clouds, we use a
155 “prescribed-observed” hybrid method in this study, in which we replace the prescribed aerosol input data with aircraft-
156 measured aerosols or idealized conditions. Note that we can only study the impact of aerosols on clouds in this
157 configuration, but not the interactive microphysical and dynamical feedback to aerosols, as model representations of aerosol
158 sink and source processes such as emissions, scavenging, and deposition are disabled in this configuration.

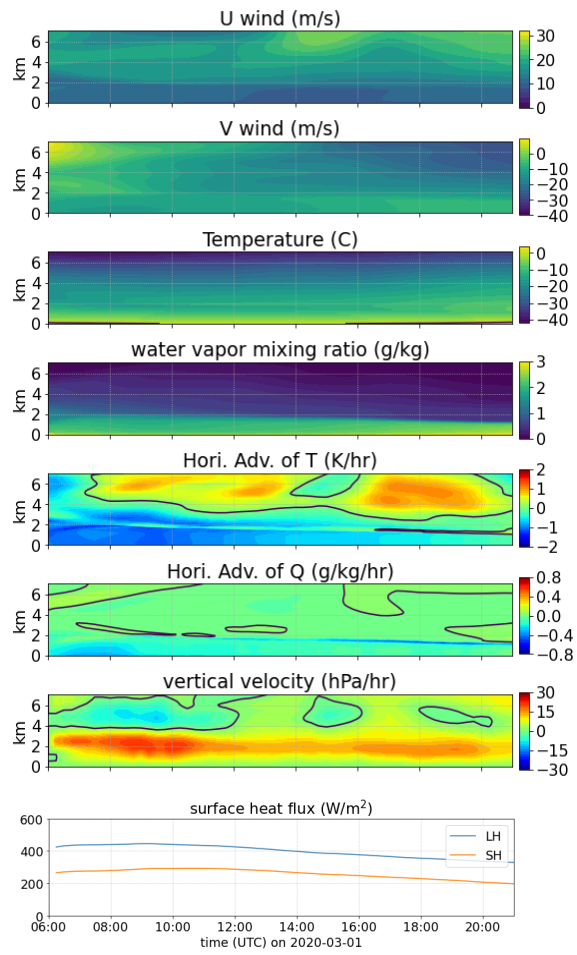
159
160 E3SM-SCM is driven by prescribed large-scale forcing data (i.e., advective tendencies and vertical velocity) and surface
161 turbulent fluxes, with a nudging timescale of 3 h to reduce biases in the atmospheric mean state. We use the same forcing
162 data as Li et al. (2022) in their WRF-LES simulations over the dropsonde region (red circle in Fig. 1a). The large-scale
163 forcing fields are shown in ~~the left panel of~~ Fig. 2. The environment exhibits strong subsidence with cold and dry advection
164 in the lower atmosphere. The near-surface cold and dry air and relatively high SST (not shown) lead to large surface latent (~
165 400 W/m²) and sensible (> 200 W/m²) heat fluxes. Although these data are obtained from the ERA5 reanalysis, which
166 exhibits a cold and dry bias in MBL (Seethala et al., 2021), the wind structure is well captured (Chen et al., 2022) and the
167 ERA5 divergence agrees well with that derived from the ACTIVATE dropsonde array (Li et al., 2022). Overall, it has been
168 shown that the ERA5-derived large-scale forcing and surface turbulent fluxes can reasonably reproduce clouds and boundary
169 layer for this case in WRF-LES simulations (Li et al., 2022; Li et al., 2023).

170
171 The WRF-CRM (Chen et al., 2022) and WRF-LES (Li et al., 2022; Li et al., 2023) simulations are also used for
172 intercomparison with the E3SM-SCM. The WRF-CRM has an outer domain at a 3 km horizontal grid and an inner domain
173 ~~in~~ at a 1 km convective-resolving resolution, with an interactive land option and prescribed SST from ERA5. It is able to
174 reproduce the “cloud street” feature seen in satellite images (Chen et al., 2022). The comparison of WRF-CRM nested

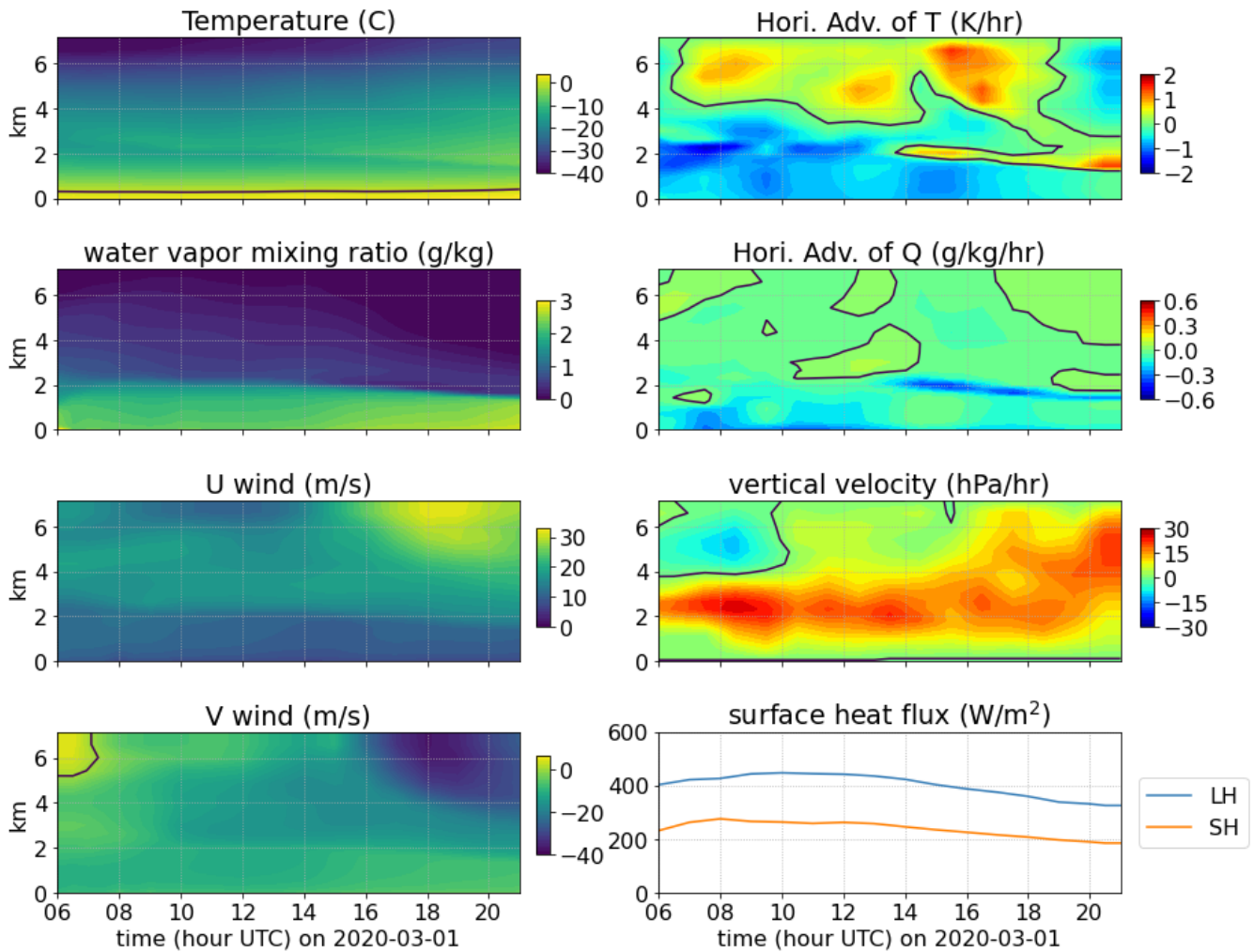
175 ~~simulation with ERA5 reanalysis over the dropsonde region and the results~~ impact of using them to drive ~~results of SCM and~~
176 ~~LES, driven by WRF-CRM forcings, are given in the Supplement Information~~ Supplement Information (Figs. S1-S4). ~~S1-~~
177 ~~S4). Over the dropsonde region, the nested WRF-CRM simulation shows stronger cold advection in MBL and weaker~~
178 ~~subsidence above MBL (the right panel of Fig. 2) than the ERA5 large scale forcing. The near surface temperature and~~
179 ~~moisture in WRF-CRM are lower than ERA5, yielding higher surface latent (21–68 W/m² higher) and sensible (26–55 W/m²~~
180 ~~higher) heat fluxes.~~ The WRF-LES simulation has a domain size of 60x60 km² with a 300 m horizontal grid spacing (Li et
181 al., 2022). Its large-scale forcing and surface turbulent fluxes are prescribed from ERA5, as described above. Nudging is
182 applied only to horizontal winds at a timescale of 1 h, with temperature and moisture freely evolving. In both CRM and LES
183 simulations, a uniform cloud droplet number concentration (N_d) was specified so ACI processes ~~are~~ were bypassed. The
184 specified N_d value of 450 cm⁻³ was obtained from a previous version of FCDP measurements (Li et al., 2022). The newer
185 version of FCDP (see Table 1) with an updated d instrument calibration gives a smaller N_d value. As will be seen later (e.g.,
186 Fig. 5), the E3SM-SCM simulation is more consistent with the updated FCDP data. Note that ~~here~~ we keep the original
187 setups of prescribed N_d in CRM and LES for consistency with previous studies (Chen et al., 2022; Li et al., 2022; Li et al.,
188 2023). As all the simulations are available for the same case, we have the opportunity to demonstrate the value of combining
189 CRM and LES with SCM for the process-level understanding of ACI.



ERA5



WRF-CRM



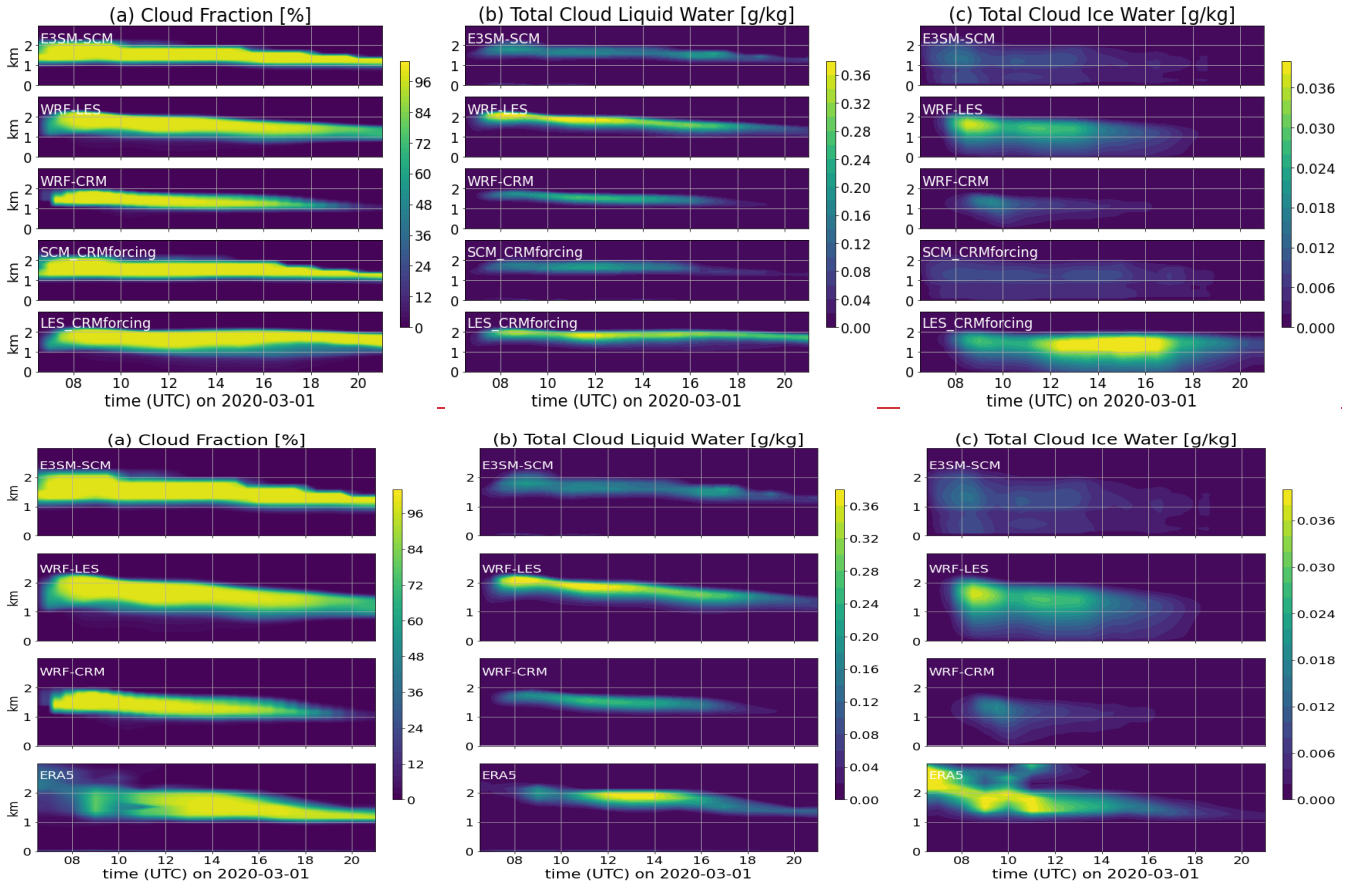
191

192 **Figure 2: Large-scale environmental conditions, large-scale forcing (horizontal advection and vertical velocity), and surface**
 193 **forcings (latent and sensible heat fluxes) over the dropsonde region from ERA5 reanalysis, used in SCM and WRF-LES (left) and**
 194 **from the WRF-CRM simulations (right). The black lines in large-scale forcing panels mark the zero contour.**

195 **3 SCM performance and intercomparison with /CRM/LES intercomparison**

196 All the E3SM-SCM, WRF-LES, and WRF-CRM simulations are initiated at 06:00 UTC, 1 March 2020. With a quick initial
 197 spin-up, marine CAO clouds develop between 1 and 2 km above ground level (AGL), and then display a gradual reduction in
 198 vertical extent, cloud top height, and cloud water content (Figs. 3 and 4). These are generally consistent with ERA5
 199 reanalysis. Note, ~~Noting that the ERA5 cloud properties are also obtained~~ output obtained from the reanalysis host model.
 200 Both SCM and WRF-LES generate a-100% cloud fraction most of the time, while the WRF-CRM simulated cloud fraction
 201 decreases with time. This is associated with the success of capturing cloud roll structure in WRF-CRM (Chen et al., 2022).
 202 However, this roll structure fails to be simulated in WRF-LES and is not ~~neither resolved nor~~ not parameterized at the sub-

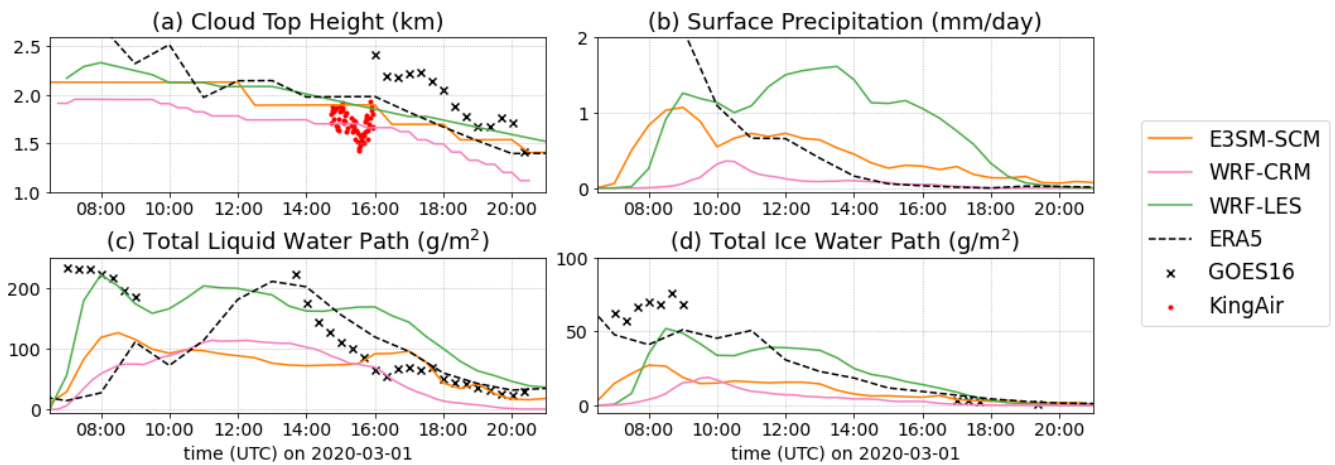
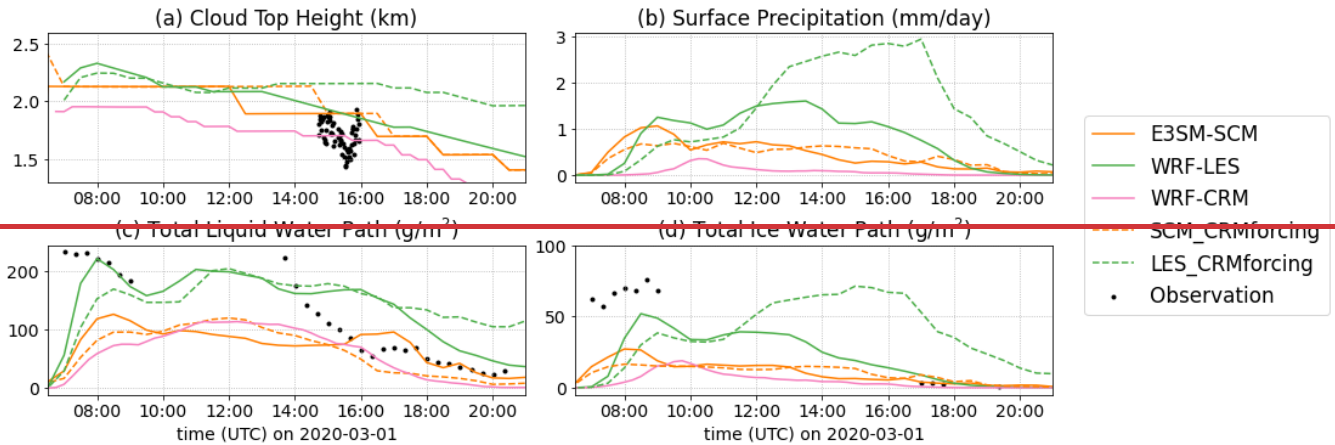
203 ~~grid scale~~ in E3SM-SCM. Both liquid and ice hydrometeors are produced and transformed into rain and snow particles. The
 204 total ice (including snow) water content is about one order of magnitude smaller than total liquid water (including rain) (Fig.
 205 3b and 3c). In our further analyses, we ignore ice and only focus on liquid clouds for simplicity. All simulations produce a
 206 weak mean surface precipitation of less than 2 mm/day (Fig. 4b, 4b), ~~except an LES sensitivity experiment discussed later.~~
 207 The evaluation of surface precipitation versus observations is not conducted here due to the lack of surface measurements
 208 and the limited ability of satellite measurements ~~to detect in detecting~~ weak precipitation from low-level MBL clouds (e.g.,
 209 Battaglia et al., 2020).



211
 212 **Figure 3: Time-height cross-sections of cloud fraction, total liquid water, and total ice water produced from different model**
 213 **simulations.**

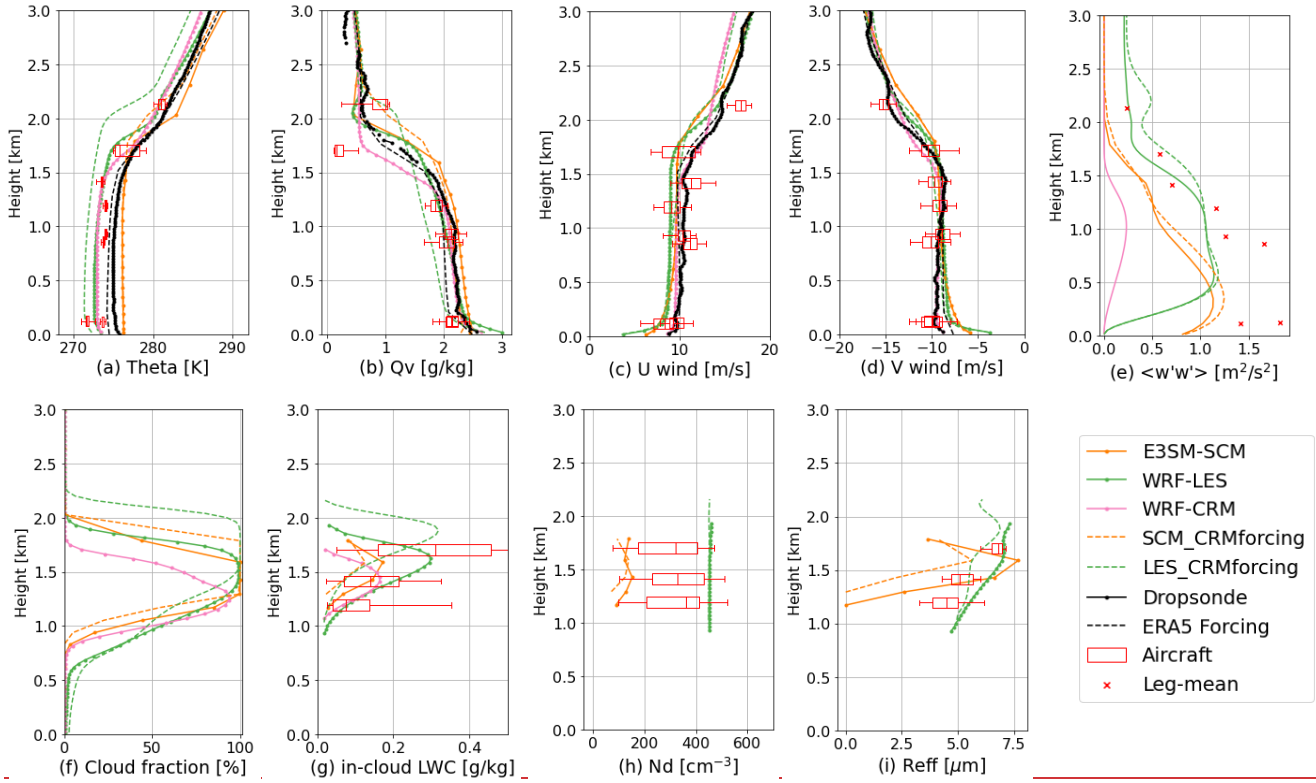
214
 215 Figure 4a shows the time series of cloud top height compared with GOES-16 satellite measurements and HSRL-2
 216 measurements from the King Air aircraft. ~~It should be noted that although both are measured from above the cloud, the~~
 217 ~~satellite-measured cloud top height is about 1 km higher than the aircraft lidar measurement. As this is only a case study, we~~
 218 ~~do not attempt to address whether the satellite measurement has any systematic bias. HSRL-2 detects the top of each~~

219 individual cloud, which is usually lower than or, at best, equal to the highest cloud top within the area. Therefore, we only
 220 compare model results with the highest values of the HSRL-2 measurements. The cloud top heights in models are derived by
 221 integrating cloud-fraction-weighted height levels downward, as described in Varble et al. (2023). E3SM-SCM and WRF-
 222 LES produce similar cloud top heights (Fig. 4a), consistent with the highest observed cloud tops in HSRL-2, 4a), consistent
 223 with the highest observed cloud tops in HSRL-2 ~~but a few hundred meters higher than most of the aircraft in-situ~~
 224 ~~observations during the time of operation. It should be noted that HSRL-2 detects the top of each individual cloud, which is~~
 225 ~~usually lower than or, at best, equal to the highest cloud top within the area. Therefore, this result indicates that cloud top~~
 226 ~~height is reasonably simulated in the three models, although the HSRL-2 measurements indicate a strong spatial variability.~~
 227 Ignoring the model spin-up period and high solar zenith angle when satellite retrievals encounter large biases, E3SM-SCM
 228 and WRF-CRM also reproduced the total liquid water path, while WRF-LES overestimates it by ~50% after 14:00 UTC,
 229 compared to the satellite retrievals (Fig. 4c). For the total ice water (including snow), with only a few valid data points in
 230 GOES-16 retrievals around 17:00 UTC, SCM and LES seem to overestimate it, albeit the overall magnitude is small (Fig.
 231 4d).

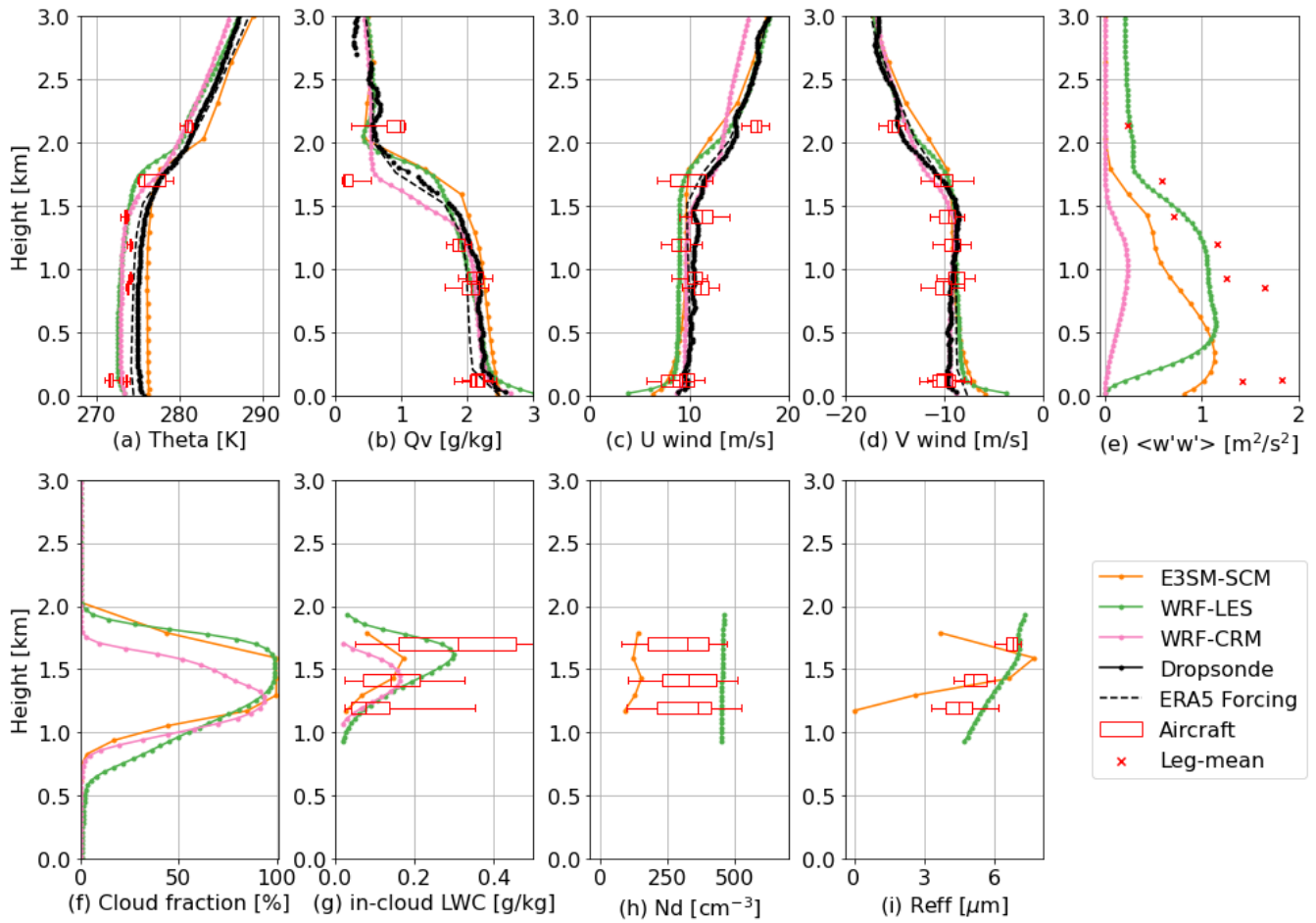


234
235
236

Figure 4: Time series of model simulations (lines) compared with observation (dots) for the 01 March 2020 case. Observational data are from the King Air HSRL-2 for cloud top height, and GOES-16 retrievals for cloud top height, total liquid (including rain) and total ice (including snow) water paths, for which data points at solar zenith angle greater than 65° are removed.



237



238

239 **Figure 5: Vertical profiles of atmospheric state, vertical velocity variance, and cloud variables over the analysis domain compared**
 240 **with dropsonde and Falcon measurements. Model profiles are averaged between 15:00 and 16:00 UTC during the aircraft**
 241 **measurements. The box plots indicate the interquartile ranges of the aircraft measurements in each flight leg and the whiskers**
 242 **indicate 5th and 95th percentiles, while the red crosses represent vertical velocity variances calculated from 1 Hz measurements in**
 243 **each flight leg. For cloud microphysical variables, a threshold of in-cloud liquid water content of 0.02 g/m³ and cloud droplet**
 244 **number of 20 cm⁻³ is applied for both model results and aircraft measurements.**

245 Figure 5 shows the vertical profiles of atmospheric state and cloud variables compared to dropsondes, ERA5 forcing data,
 246 and in-situ aircraft measurements. The atmospheric state variables are constrained by ERA5 reanalysis, which has a colder
 247 and dryer boundary layer than the dropsonde measurements (Figs. 5a and 5b, as well as reported in Seethala et al., 2021).
 248 However, the Falcon data in the boundary layer are also colder and dryer than the dropsonde measurements. These
 249 differences reflect observational uncertainties to some extent. All models are generally consistent with the observations.
 250 However, they do show different temperature biases: E3SM-SCM tends to be warmer while WRF-LES and WRF-CRM tend
 251 to be colder than the dropsondes. This bias is seen throughout the entire simulation period (not shown), indicating different
 252 performances of model parameterizations in E3SM-SCM and WRF-LES, as they used the same initial conditions and large-
 253 scale forcing.

254

255 WRF-LES and WRF-CRM both use prescribed N_d obtained from a previous version of Falcon aircraft measurements during
256 the ACB flight leg, which is higher than the re-calibrated value in the current version (Fig. 5h). They produce similar in-
257 cloud liquid water content (LWC) below 1.5 km, but WRF-CRM produces lower LWC above 1.5 km because of its lower
258 cloud top height (Fig. 5g). WRF-LES produces slightly greater droplet effective radius (R_{eff}) than aircraft measurements (Fig.
259 5i). Together with the large N_d , both contribute to large cloud LWC and LWP. WRF-CRM uses bulk microphysics and does
260 not have R_{eff} . The E3SM-SCM simulated LWC is consistent with aircraft measurements during the BCT2 flight leg near 1.4
261 km AGL, but lower than the other two in-cloud flight legs (Fig 5g). It also produces larger sizes of cloud droplets around 1.5
262 km AGL (Fig. 5i); but produces much lower N_d (Fig. 5h). Possible causes of the underestimation of N_d include an
263 underestimation of both aerosol number concentration (see Sect. 4.1) and weaker turbulence (Fig. 5e). The lower N_d is partly
264 due to the smaller vertical velocity variance in the SCM simulations compared to the aircraft measurements (Fig. 5e),
265 suggestive of weaker updraft velocity causing weaker vertical velocity variance than observations. Observation is a general
266 bias seen in E3SM for the entire ACTIVATE campaign (Brunke et al., 2022), which and may cause lower supersaturation
267 (SS) which activates fewer cloud condensation nuclei (CCN) into cloud droplets (e.g., Kirschler et al., 2022). We
268 Another reason is the use of climatological aerosols as input, which provides too low CCN concentrations for this case. As will be
269 seen We will further investigate these two factors in Sect. 4.1.4.1, using observed aerosols brings N_d much closer to the
270 observations.

271

272 ~~The differences in large scale forcing and surface turbulent fluxes between ERA5 and WRF CRM (Fig. 2) raise a question~~
273 ~~of how the large scale forcing impacts the simulations in E3SM SCM and WRF LES, considering that WRF CRM and~~
274 ~~E3SM SCM/WRF LES show many similarities in simulated cloud properties. To answer this, we configure E3SM SCM and~~
275 ~~WRF LES with the large scale forcing and surface fluxes from WRF CRM over the dropsonde domain (shown in the right~~
276 ~~panel of Fig. 2) to conduct two simulations, referred to as SCM_CRMforcing and LES_CRMforcing, respectively. Results of~~
277 ~~these two simulations are included as dashed lines in Figs. 3-5. Because of the stronger cold and dry air advection and~~
278 ~~weaker subsidence, both SCM_CRMforcing and LES_CRMforcing simulations generate a colder, dryer, and deeper~~
279 ~~boundary layer (Figs. 5a and 5b), especially for LES_CRMforcing in which temperature and moisture are not nudged. The~~
280 ~~cloud layers in both models are overall thicker than using the ERA5 forcing (Fig. 3a), but detailed features are different~~
281 ~~between SCM and LES. Compared to the E3SM SCM, SCM_CRMforcing follows the same trend of cloud top reduction~~
282 ~~rate (Fig. 4a), with a little time lag. Therefore, the cloud grows higher between 15:00 and 16:00 UTC (Fig. 5f) but has~~
283 ~~smaller LWC and R_{eff} (Figs. 5g and 5i). For LES, the cloud top height in LES_CRMforcing reduces with a slower rate (Fig.~~
284 ~~4a), causing a ~500 m higher cloud top between 15:00 and 16:00 UTC (Fig. 5f). Because of the colder temperature, more~~
285 ~~cloud hydrometeors are converted to the ice phase (Figs. 3c and 4d), with more precipitation falling to the ground (Figs. 4b).~~
286 ~~This sensitivity study shows a large impact of the large scale forcing and surface fluxes on cloud properties in the SCM and~~

287 ~~LES simulations. A proper combination of large-scale dynamics, sub-grid scale parameterizations, and model configurations~~
288 ~~is needed to obtain optimal performance in simulating MBL clouds.~~

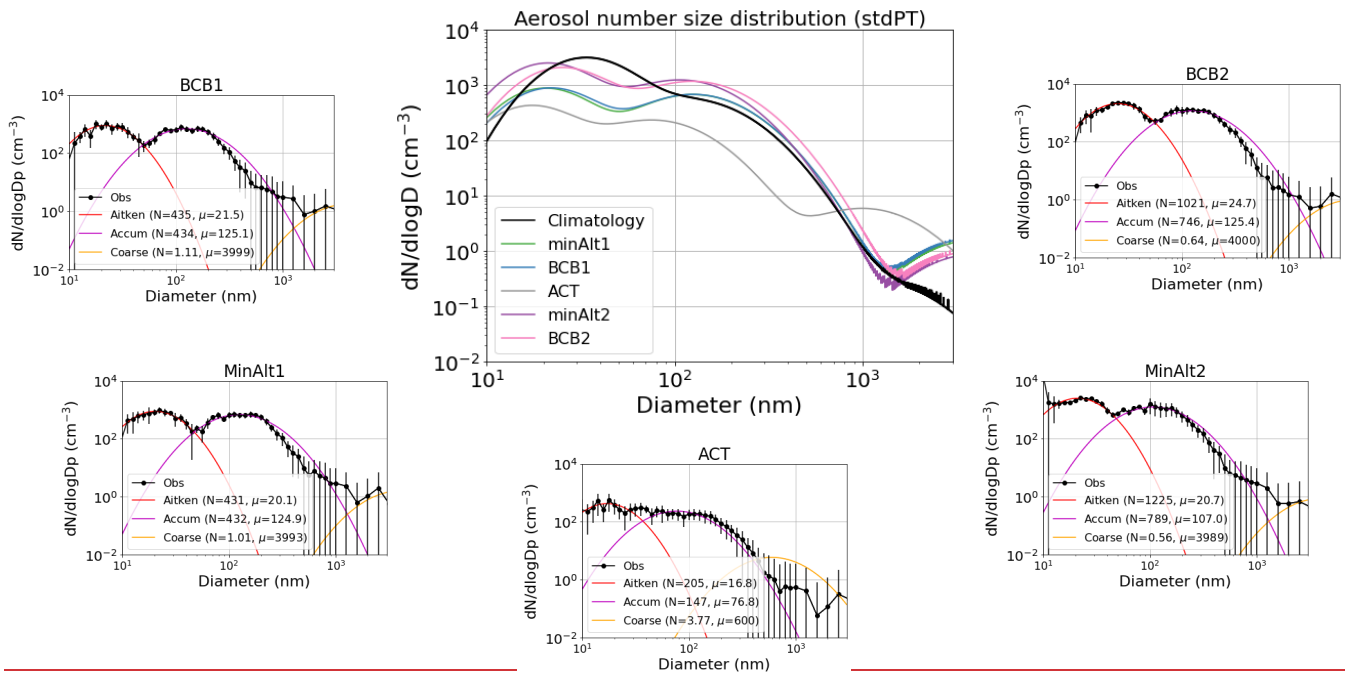
289 4 SCM Sensitivity Tests

290 The previous section suggests that the underestimation of N_d in E3SM may be partly due to the underestimation of aerosol
291 number concentration in the climatological aerosol input for this CAO case. In this section, we use observed aerosols to
292 drive E3SM-SCM and conduct two sets of sensitivity studies on aerosol number size distribution and composition to
293 investigate how the input aerosol properties impact clouds and ~~the~~ radiative forcings.

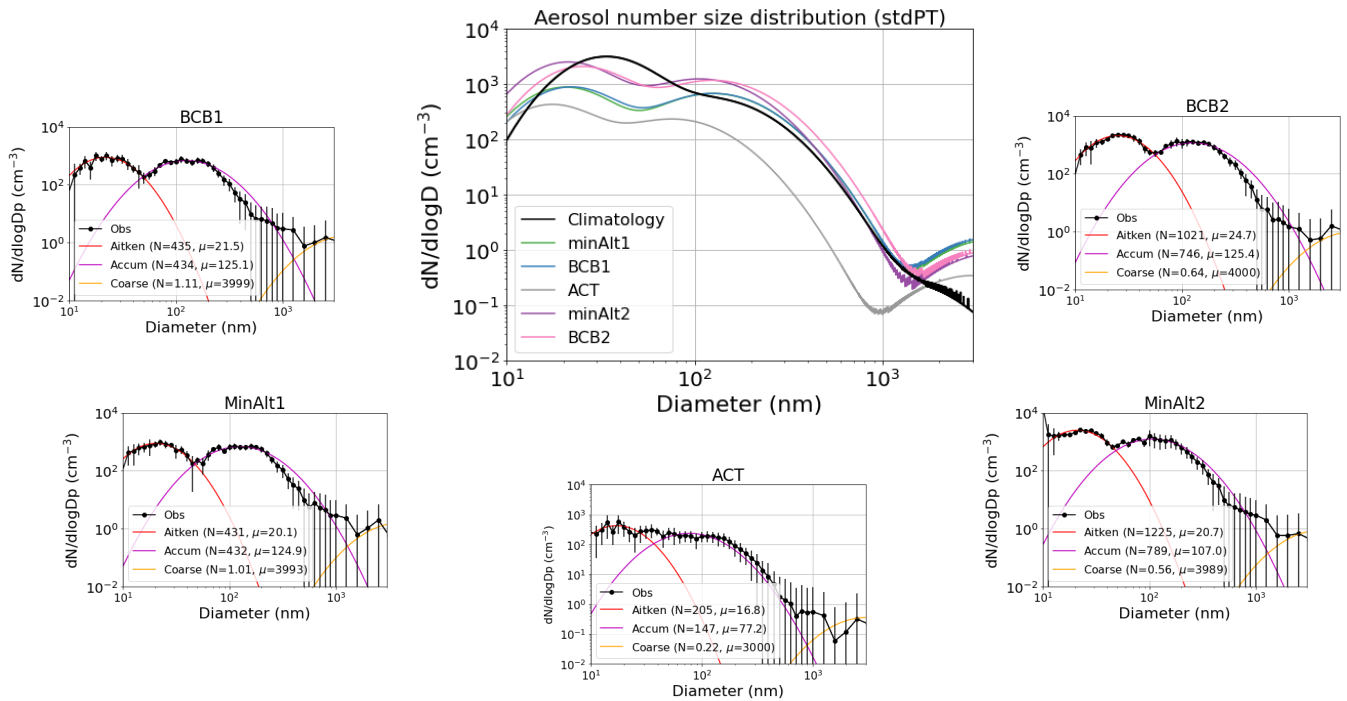
294 4.1 Sensitivity to different aerosol number size distributions

295 We firstly test the sensitivity of SCM simulations to different aerosol number size distributions using the measurements from
296 five out-of-cloud legs within or near the dropsonde domain (Fig. 1b). The Falcon aircraft during the ACTIVATE campaign
297 was equipped with ~~an~~ SMPS and ~~an~~ LAS (Table 1) to measure aerosol number size distribution from 2.97 to 94.0 nm (for
298 SMPS) and 93.9 to 3487.5 nm (for LAS), respectively. We merge the two instruments and fit them into three lognormal
299 modes: Aitken, accumulation, and coarse modes. For the three parameters in the lognormal distribution function: mode total
300 number concentration (N), mode geometric median diameter (μ), and standard deviation (σ_g), we only fit N and μ . Because
301 σ_g is also prescribed in other parts of the model (e.g., radiation calculation), we fix σ_g with the E3SM-prescribed values (1.6
302 for Aitken, 1.8 for accumulation and coarse) for consistency. A sensitivity test shows that using freely fitted N, μ , and σ_g in
303 E3SM-SCM only yields a minor difference compared to using fixed σ_g (not shown). For most flight legs, the fitting of
304 ~~coarse-coarse-mode aerosols encountered-exhibits~~ large uncertainties due to ~~too few~~ limited samples ~~and-with~~ large
305 variation, variations. As the coarse mode aerosol number concentration is usually orders of magnitude smaller than that of
306 the Aitken and accumulation modes, the poor fitting of coarse mode aerosols is not expected to impact the cloud
307 microphysical properties much.

308
309 The centre panel of Fig. 6 shows the fitted aerosol number size distributions from different flight legs, overlapped with
310 E3SM climatological aerosols near the cloud base height (~ 900 m AGL). The individual fitting of the three modes as well as
311 the fitting parameters in each flight leg are shown in the surrounding panels. It is clearly seen that the below-cloud flight legs
312 (minAlt and BCB) generally have more aerosols, especially in the accumulation mode, than the above-cloud-top flight leg
313 (ACT). The E3SM climatological aerosols at the cloudBCB2-level ~~cloud base~~ show more and larger Aitken mode particles
314 and less coarse mode particles than all flight leg measurements. For accumulation mode particles that are most important for
315 CCN number concentration, the E3SM climatology lies between the ACT leg and below-cloud legs. Although the ACT leg
316 does not represent cloud-base aerosol conditions that are more relevant to the aerosol activation process, the inclusion of this
317 leg provides information of-on how SCM performs in a clean environment.



318



319

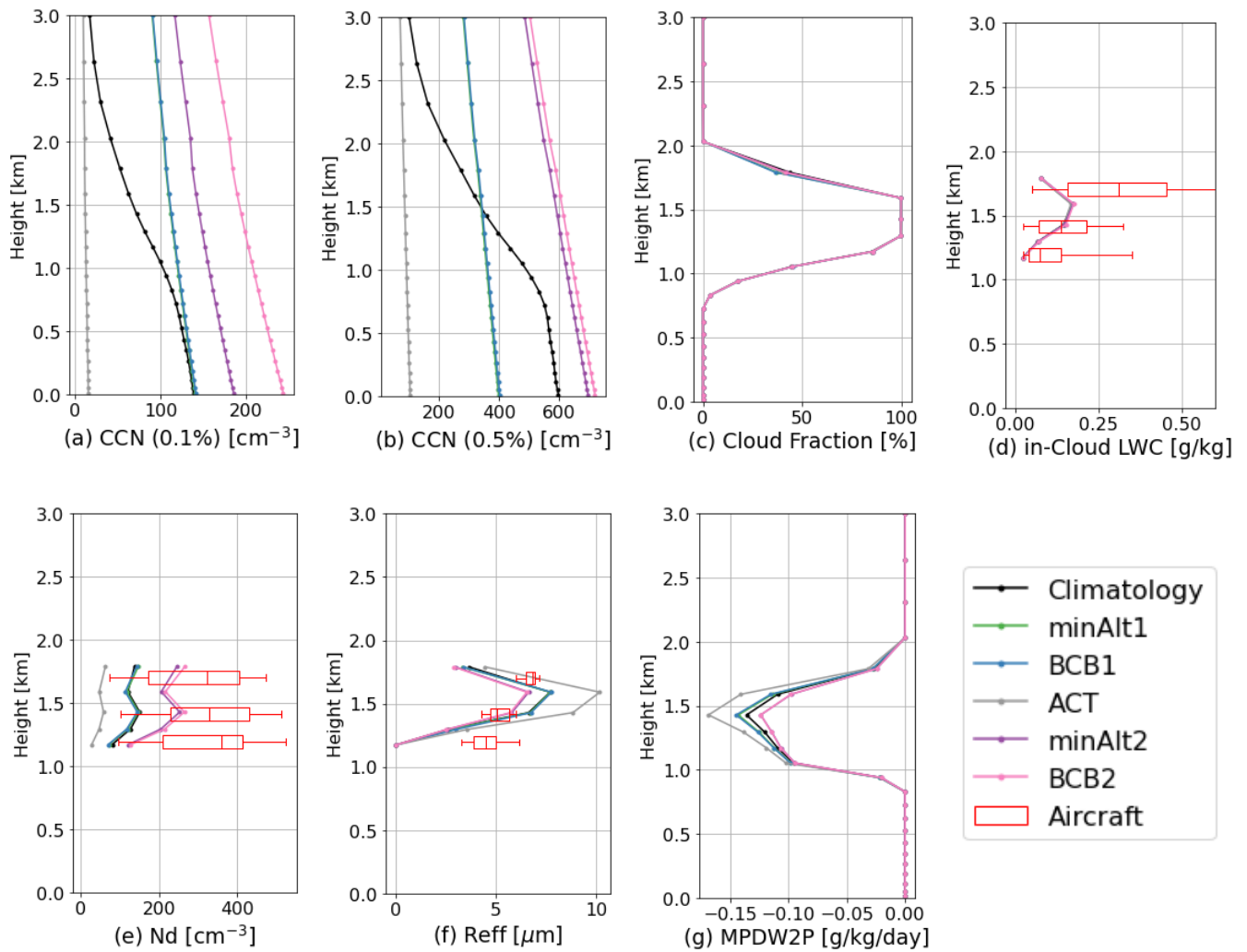
320 **Figure 6:** (centre) Aerosol number size distribution from (black) E3SM prescribed aerosol file from climatological run
 321 near the height of simulated cloud base (~900 m AGL) and (colours) aircraft measurements averaged for each out-of-cloud flight
 322 leg fitted to 3-mode lognormal distributions. (surroundings) Mean observed aerosol number size distribution and one standard
 323 deviation (vertical lines) from each out-of-cloud flight leg and the lognormal fittings for Aitken, accumulation, and coarse modes.
 324 The fitting parameters (N in cm^{-3} and μ in micrometres) are shown in the figure legends with the geometric standard deviation (σ_g)

325 set as 1.6 for Aitken mode and 1.8 for accumulation and coarse modes. All data are converted for standard pressure (1013.25 hPa)
326 and temperature (273.15 K) conditions.

327 The fitted lognormal parameters from aircraft measurements are used to calculate and replace the variables in the E3SM--
328 prescribed aerosol input data. The averaged chemical component fractions below 1.5 km from E3SM aerosol climatology are
329 used to partition the measured aerosol number size distribution so they all have the same fraction of aerosol components. The
330 sensitivity to different aerosol chemical compositions will be discussed in Sect. 4.2, while in this section we only focus on
331 how aerosol number concentration impacts clouds in E3SM-SCM. The prescribed aerosol number concentration has no
332 information ~~on~~ variation with height. This height-independent assumption is usually used in SCM configurations with
333 observed aerosols (e.g., Liu et al., 2007; Klein et al., 2009; Liu et al., 2011), assuming that only cloud-base aerosols are
334 involved in the cloud droplet nucleation processes (e.g., Liu et al., 2011). ~~Nonetheless, we also conduct a sensitivity study on~~
335 ~~aerosol vertical distributions in Sect. 4.3.~~

337 ~~All simulations are run from 06:00 to 21:00 UTC, the same as the previous simulations in Sect. 3. To compare with aircraft~~
338 ~~measurements, we average the simulations between 15:00 and 16:00 UTC (aircraft sampling time) and plot the vertical~~
339 ~~profiles in Figure-Fig. 7. (a-f) shows the vertical profiles of aerosol and cloud properties from the E3SM SCM aerosol~~
340 ~~sensitivity simulations between 15:00 and 16:00 UTC. The large variation of CCN number concentrations~~ has a very small
341 impact on the cloud fraction and in-cloud LWC. Instead, it mainly impacts the cloud droplet number and size: more CCN
342 ~~number concentration~~ leads to more N_d and smaller droplet size. However, all the simulations underestimate N_d compared to
343 the aircraft measurements. ~~A further~~ Another sensitivity test shows that both underestimation of both aerosol number
344 concentration and underestimation of turbulence strength contributes to the underestimation of N_d . When increasing vertical
345 velocity variance to the observed magnitude and using aerosols observed below the cloud base in aerosols into drive SCM,
346 the simulated N_d is then becomes much closer more similar to the aircraft measurements (Fig. 8).

348 ~~We further plot the simulated cloud droplet number size distribution at three different heights in Fig. 9, with different~~
349 ~~simulations using prescribed aerosols from different flight legs. As seen in Fig. 8, Compared with the aircraft-measured~~
350 ~~cloud droplet size distribution at each height, the gamma distribution assumption of the cloud droplet spectrum in MG2~~
351 generally captures the observed droplet size distribution and reproduces well the mean droplet size, but fails to reproduce the
352 observed peak of N_d at all three heights. A similar sharp peak of N_d around 10 to 20 μm was also observed by aircraft over
353 the Southern Ocean and the model with the same MG2 microphysics scheme underestimated N_d in a similar way (Gettelman
354 et al., 2020). ~~Since observed aerosols are used to drive the SCM simulations, the underestimation of N_d indicates that the~~
355 ~~turbulence in SCM is likely too weak that produces lower supersaturation thus cannot activate enough aerosols into cloud~~
356 ~~droplets. This is confirmed by the evidence that E3SM SCM underestimates vertical velocity variance when compared to the~~
357 ~~Falcon measurements (Fig. 5e), and is a general bias seen in the entire ACTIVATE campaign (Brunke et al., 2022).~~



359

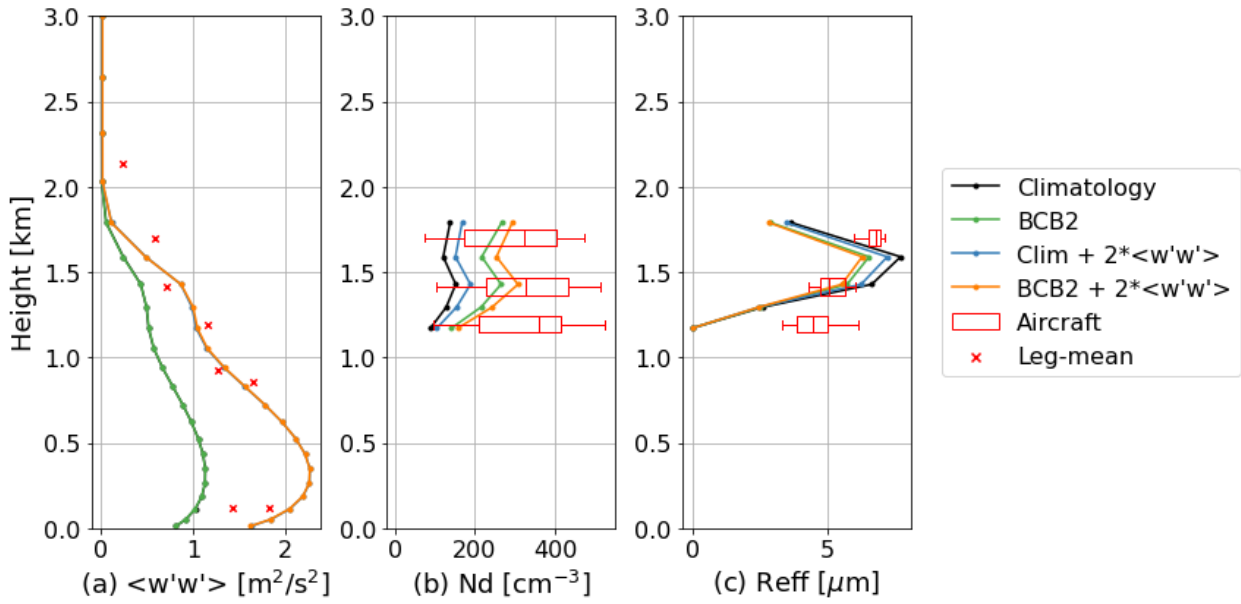
360

361

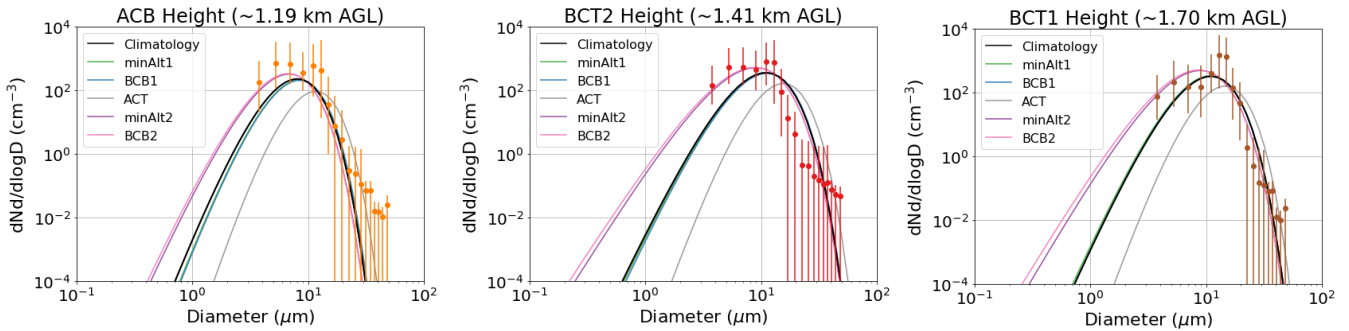
362

363

Figure 7: Vertical distributions of (a) CCN number concentrations at 0.1% and (b) 0.5% supersaturation, (c) cloud fraction, (d) in-cloud LWC, (e) N_d , (f) R_{eff} , and (g) cloud water tendency from the conversion-to-precipitation processes (MicroPhysics tendency Due to Water to Precipitation, MPDW2P) in E3SM-SCM simulations with different aerosol specifications. Aircraft measurements of cloud microphysical properties overlaid are the same as in Figure 5.



364
 365 **Figure 8: (a) Vertical velocity variance $\langle w'w' \rangle$, (b) cloud droplet number concentration N_d , and (c) cloud droplet effective**
 366 **radius R_{eff} averaged between 15:00 and 16:00 UTC, when the aircraft measurements (shown in red crosses and boxes) were made.**
 367 **In the figure legend, “Climatology” is the original SCM run with prescribed aerosol concentration; “BCB2” is SCM run with**
 368 **aerosol number concentration from the aircraft measurement at BCB2 leg; and “ $2*\langle w'w' \rangle$ ” means the vertical velocity variance**
 369 **is enhanced by the factor of 2 in the SCM aerosol activation scheme.**
 370

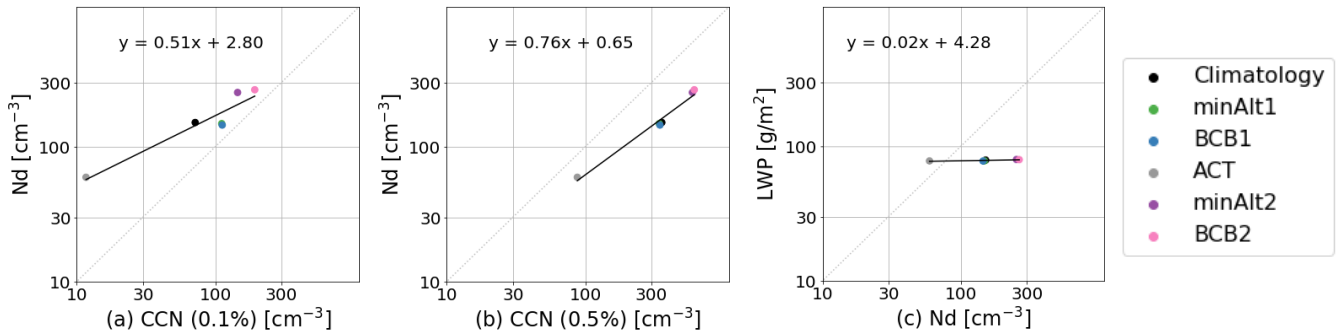


371
 372 **Figure 989: E3SM-SCM simulated cloud droplet size distribution at the height of three in-cloud flight legs (ACB: ~1.20 km, BCT2:**
 373 **~1.44 km, BCT1: ~1.74 km). Note that the flight leg name and height in the title above each panel specify where the cloud data are**
 374 **taken for the plot, while the flight leg names within each panel legend describe where the aerosol data are taken to drive the**
 375 **corresponding E3SM-SCM simulations. The dots and error bars represent aircraft measurements at the corresponding flight legs**
 376 **and at 5th and 95th percentiles.**

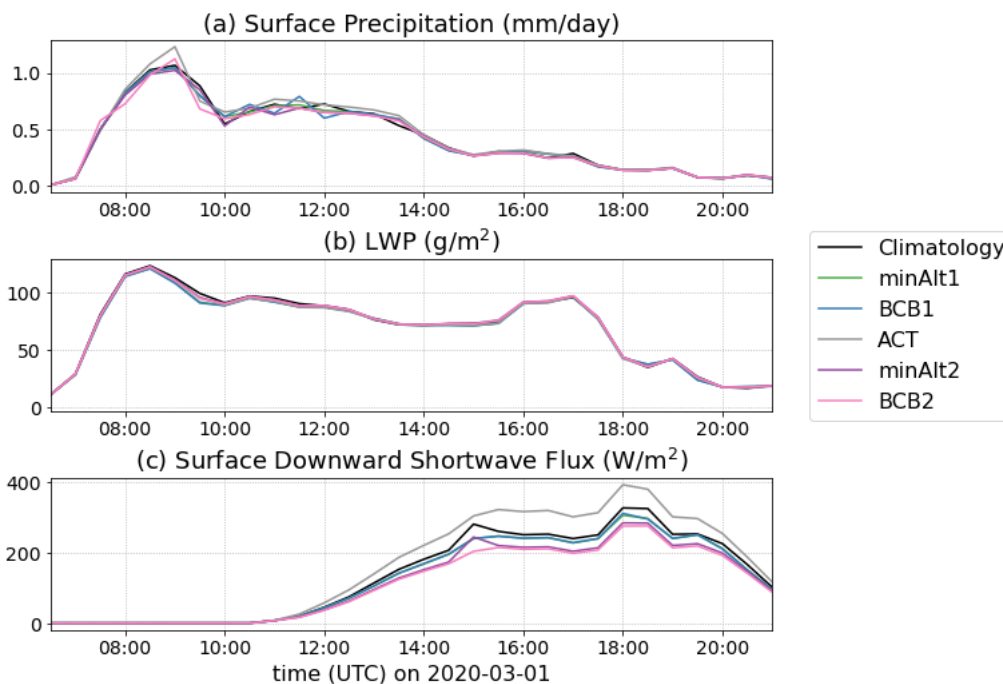
377
 378 The strong impact of aerosol number size distribution on cloud microphysical properties (number, size) in SCM indicates
 379 that E3SM shows a strong Twomey effect (Twomey, 1977, 1959). The change of N_d is tightly related to the change of CCN
 380 number concentration (Fig. 10910). A recent study of long-term E3SM simulation over the eastern North Atlantic suggests
 381 that the N_d susceptibility (i.e., $\frac{d \ln N_d}{d \ln CCN}$ relationship) in E3SM may be too strong comparing to observations (Tang et al., 2023).

382 Previous studies showed that N_d is also impacted by other factors such as updraft velocity (e.g., Kirschler et al., 2022; Chen
 383 et al., 2016), which indicates a potential need ~~to examine of examining~~ updraft velocity in E3SM in the future. The surface
 384 downward shortwave flux is largely impacted by the change of cloud droplet number and size due to different aerosol
 385 specifications (Fig. ~~11c+0e11c~~), with the differences reaching up to 100 W m^{-2} during the analysis period (15:00 – 16:00
 386 UTC).

387
 388 In contrast to the strong Twomey effect, the weak impact of aerosols on cloud macrophysical properties (cloud fraction, total
 389 water content) indicates a very weak LWP adjustment in E3SM. The LWP susceptibility $-\frac{d\ln LWP}{d\ln N_d}$ is almost zero (Fig.
 390 ~~10c109e~~). The slightly positive slope is likely due to the suppression of precipitation processes (Fig. 7g) when cloud droplet
 391 sizes decrease in ~~response~~ responses to more aerosol particles and cloud droplets ~~numbers~~. However, the magnitude of
 392 precipitation rate change is so small that it can barely change the overall LWP and surface precipitation (Fig. ~~11+011~~). ~~In the~~
 393 ~~CAO case, LWP and other cloud macrophysical properties are likely determined by the strong dynamical and~~
 394 ~~thermodynamical controls (e.g., strong cold-air advection, surface turbulent heat fluxes, and and subsidence in Fig. 2). The~~
 395 ~~change of aerosols mainly impacts cloud microphysical properties through altering cloud droplet number and size, which is~~
 396 ~~shown to have a minimum minimal effect on cloud LWP. We believe that under the synoptic conditions with weaker large-~~
 397 ~~scale forcing and/or stronger precipitation, aerosol effects on cloud macrophysical properties may be stronger.~~ This weakly
 398 linear $\frac{d\ln LWP}{d\ln N_d}$ relation in the E3SM-SCM simulations is different ~~with than~~ the non-linear $\frac{d\ln LWP}{d\ln N_d}$ relation seen in the long-
 399 term E3SM GCM run (Tang et al., 2023). ~~Whether this weak~~ $\frac{d\ln LWP}{d\ln N_d}$ ~~susceptibility is a case specific feature, the SCM~~
 400 ~~simulation constrained by large scale forcing has a lack of a feedback mechanism, or there is a large LWP – N_d covariance~~
 401 ~~with different thermodynamic conditions warrants future studies with more SCM cases or long term simulations.~~



402
 403 **Figure 10109:** Scatter plot between simulated N_d and CCN at two different supersaturations and between LWP and N_d . The linear
 404 fit equations representing $\frac{d\ln N_d}{d\ln \text{CCN}}$ and $\frac{d\ln LWP}{d\ln N_d}$ are noted in each panel. ~~The standard errors of (slope, intercept) for each panel are~~
 405 ~~(0.082, 0.37), (0.048, 0.28), (0.007, 0.037), respectively.~~



406
407 **Figure 11:** Time series of (a) surface precipitation, (b) LWP, and (c) surface downward shortwave flux from E3SM-SCM
408 simulations with different aerosol specifications.

409 4.2 Sensitivity to different aerosol composition

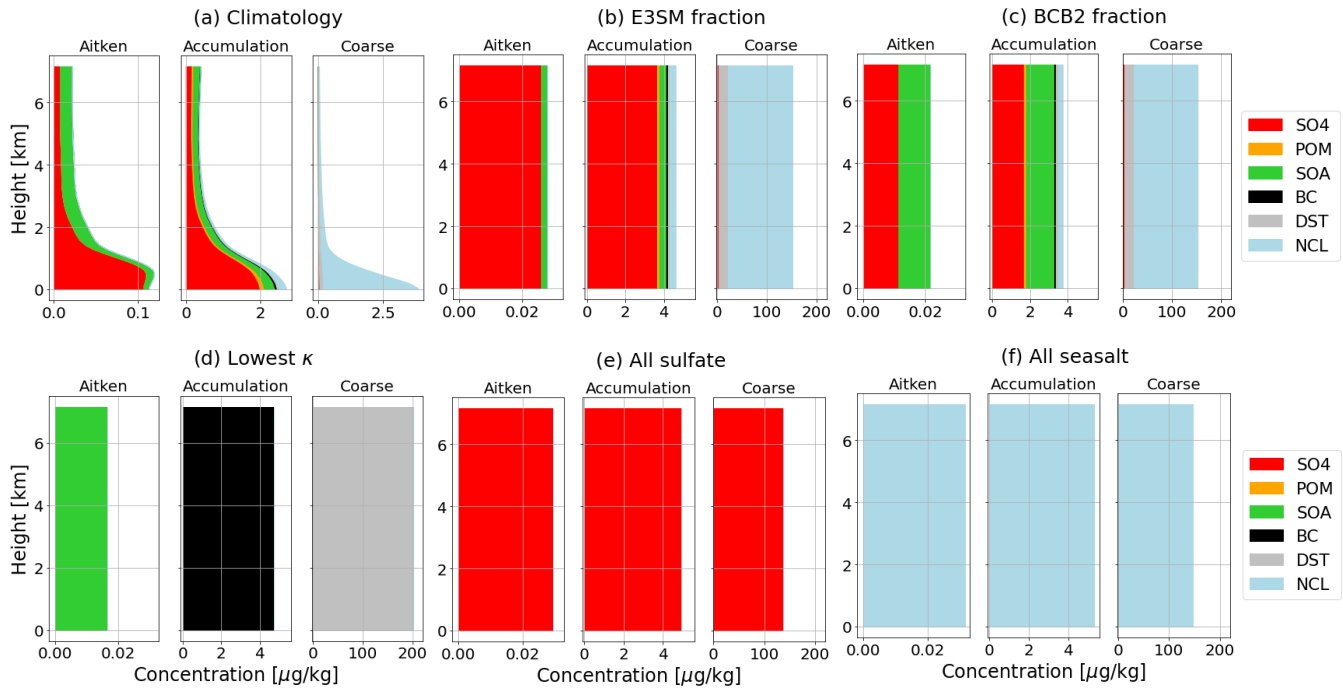
410 Aerosol chemical composition is an important property that determines the aerosol hygroscopicity (κ) and further impacts
411 the likelihood of aerosols serving as CCN and being activated into cloud droplets. In E3SM, the overall κ is
412 calculated assuming internal mixing of aerosol species within each mode and external mixing among modes (Liu et al., 2012;
413 Liu et al., 2016). Although aerosol chemical composition also impacts the overall size distribution (Shrivastava et al., 2017),
414 this mechanism is not implemented in the current E3SM. In this section, we investigate the differences of in aerosol
415 composition used in E3SM and observed by Falcon aircraft measurements. We, and further test the sensitivity of simulated
416 clouds to aerosol composition, and ultimately hygroscopicity, using simulated and observed values and assuming a few
417 extreme conditions, focusing on the change of hygroscopicity.

418
419 Figure 12a shows the aerosol mass concentrations for each component in the E3SM aerosol climatology. Most of the
420 aerosols are concentrated within the boundary layer below 1 km, with the Aitken and accumulation modes dominated by
421 sulphate, and the coarse mode dominated by sea salt aerosols. Figures 12 (b-f) all use the same observed aerosol number
422 size distribution, fitted from the BCB2 flight leg, but combined with different aerosol component fractions. The setting of
423 “E3SM fraction” uses aerosol composition from E3SM-prescribed aerosols at the level closest to the BCB2 leg (near ~900
424 m AGL). The “BCB2 fraction” uses aerosol composition from the AMS measurements at the BCB2 leg. Among the five

425 components in AMS measurements (Table 2), sulphate (SO₄) and organics are the two ~~dominated~~ dominant species
 426 observed during ACTIVATE (Dadashazar et al., 2022a). They are also the only two species specified in E3SM, with
 427 assumptions of the composition of organics. Here we assume all AMS-measured organics are secondary organic aerosols
 428 (SOA), then calculate new aerosol concentrations using the observed mass fraction of SO₄ and SOA while keeping the
 429 fraction of other species the same in E3SM. It can be seen that the aircraft measured SO₄:SOA ratio is about 1:1 in mass,
 430 much smaller than in the E3SM climatology. This change results in a reduction of κ value from 0.46 to 0.31 (Table 2) as the
 431 hygroscopicity of SOA is much smaller than SO₄.

432

433 Three other idealized aerosol settings in extreme conditions are provided for the ~~purpose of~~ sensitivity test. The first one,
 434 “Lowest κ ”, is the option to use the lowest hygroscopicity species in each mode. The second option assumes all aerosols are
 435 SO₄ aerosols and the third one assumes all sea salt aerosols. The corresponding aerosol fraction in each mode and the overall
 436 κ values are given in Table 2. The “Lowest κ ” option has an extremely low κ value of 10^{-10} in the accumulation mode, while
 437 the “all seasalt” option has a large κ of 1.16. The other options have κ values varying from 0.3 to 0.5.



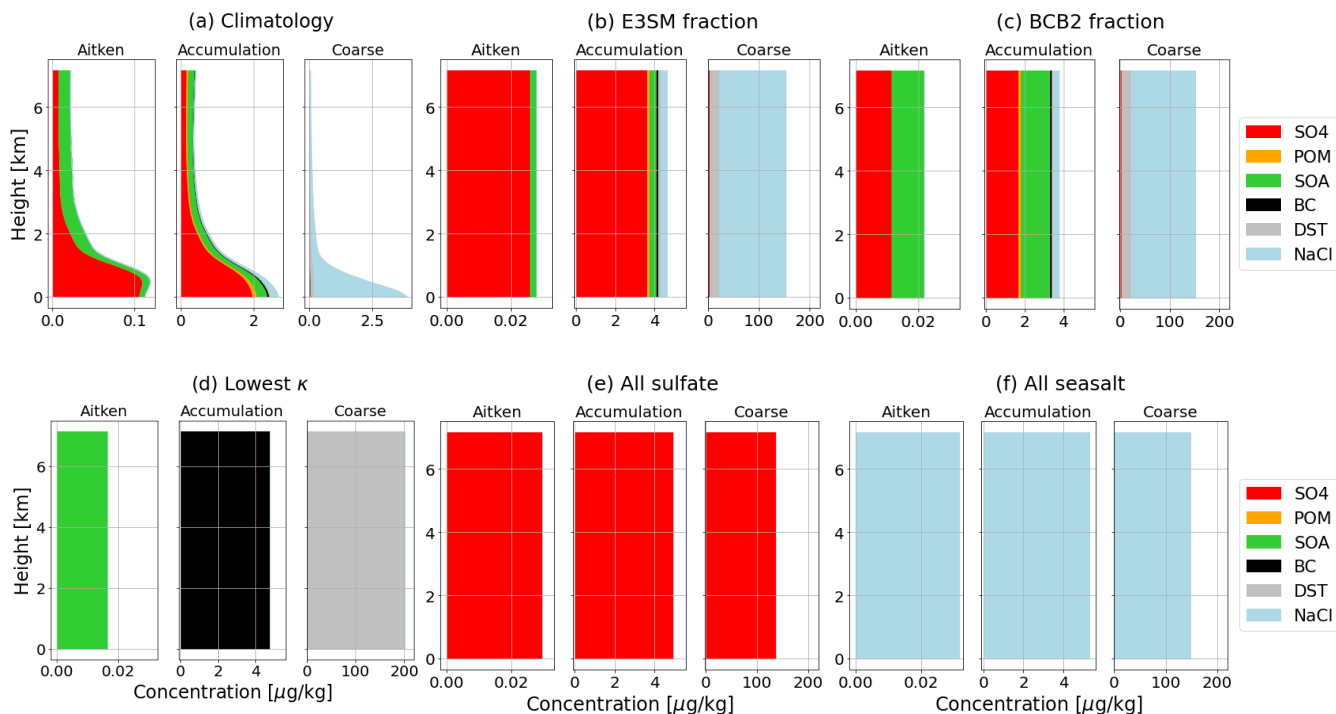


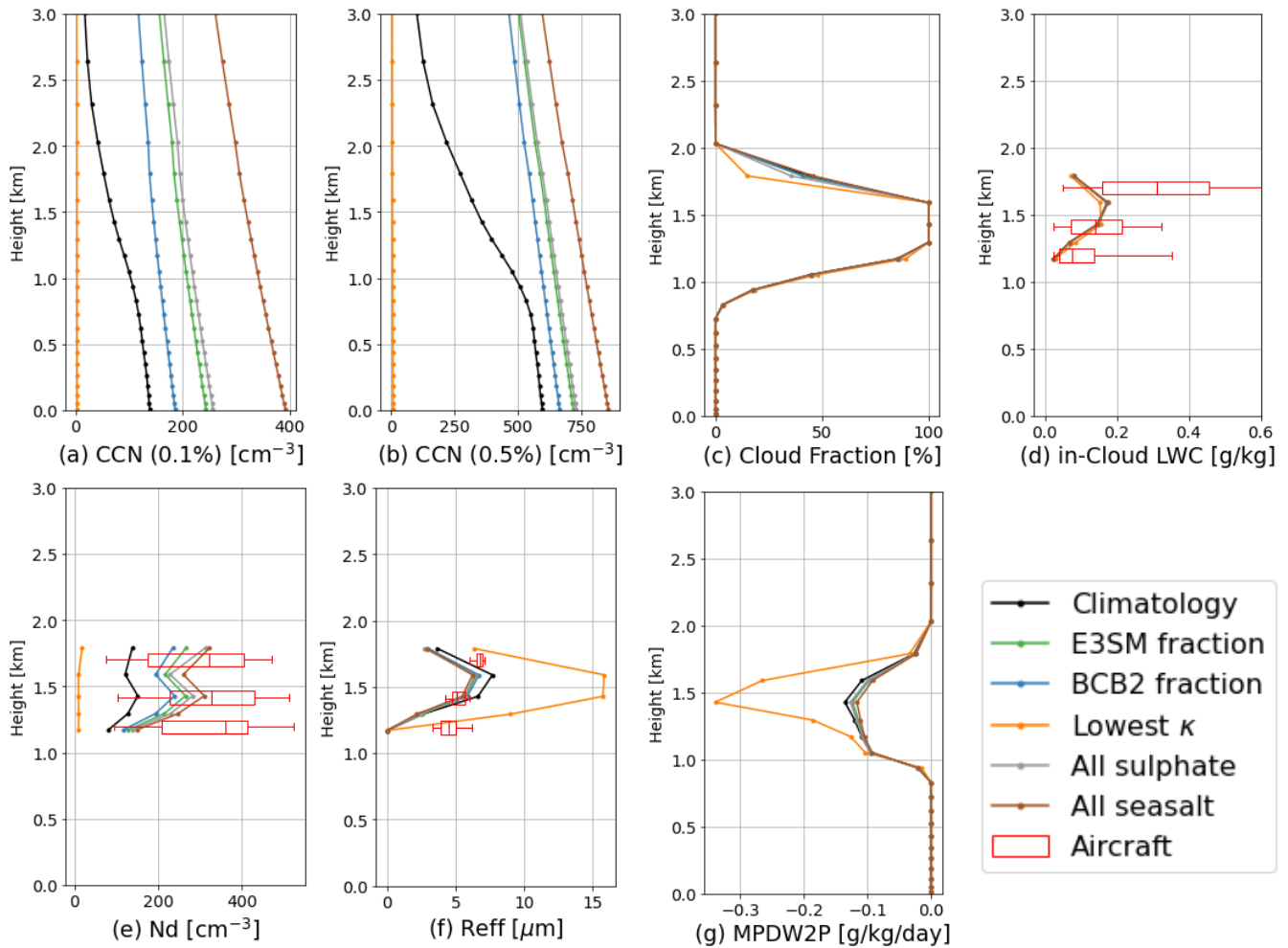
Figure 12+12: Different settings of aerosol mass concentration for each component used in E3SM from (a) climatology from E3SM GCM output, (b) applying composition fraction from E3SM climatology aerosols at the height of BCB2 flight leg, (c) using an observed fraction of sulphate and organics (assuming SOA) from the BCB2 flight leg, (d-f) assuming all aerosols are the lowest hygroscopicity species (“Lowest κ ”) in that mode, sulphate, and sea salt aerosols, respectively. Note the different x-axis in panels (a) and (b)-(f). In (b)-(f), the aerosol number size distributions are from aircraft measurements in the BCB2 flight leg and assuming no vertical variation. Notation of aerosol species: SO4: sulphate, POM: primary organic matter, SOA: secondary organic aerosols, BC: black carbon, DST: dust, ~~NaCl~~NaCl: sea salt.

Table 2: Fraction of aerosol species in each mode (Aitken/accumulation/coarse modes) specified in five sensitivity tests. “-” means the species is not accounted for in the mode.

Sensitivity test	SO4	POM	SOA	BC	DST	NaCl NaCl	κ^*
E3SM fraction	0.89/0.75/0.02	-/0.04/-	0.11/0.12/-	-/0.02/-	-/0.02/0.09	0.00/0.05/0.88	0.46
BCB2 fraction	0.39/0.34/0.02	-/0.04/-	0.61/0.53/-	-/0.02/-	-/0.01/0.09	0.00/0.05/0.88	0.31
Lowest κ	0/0/0	-/0/-	1/0/-	-/1/-	-/0/1	0/0/0	10^{-10}
All sulphate	1/1/1	-/0/-	0/0/-	-/0/-	-/0/0	0/0/0	0.507
All sea salt	0/0/0	-/0/-	0/0/-	-/0/-	-/0/0	1/1/1	1.16

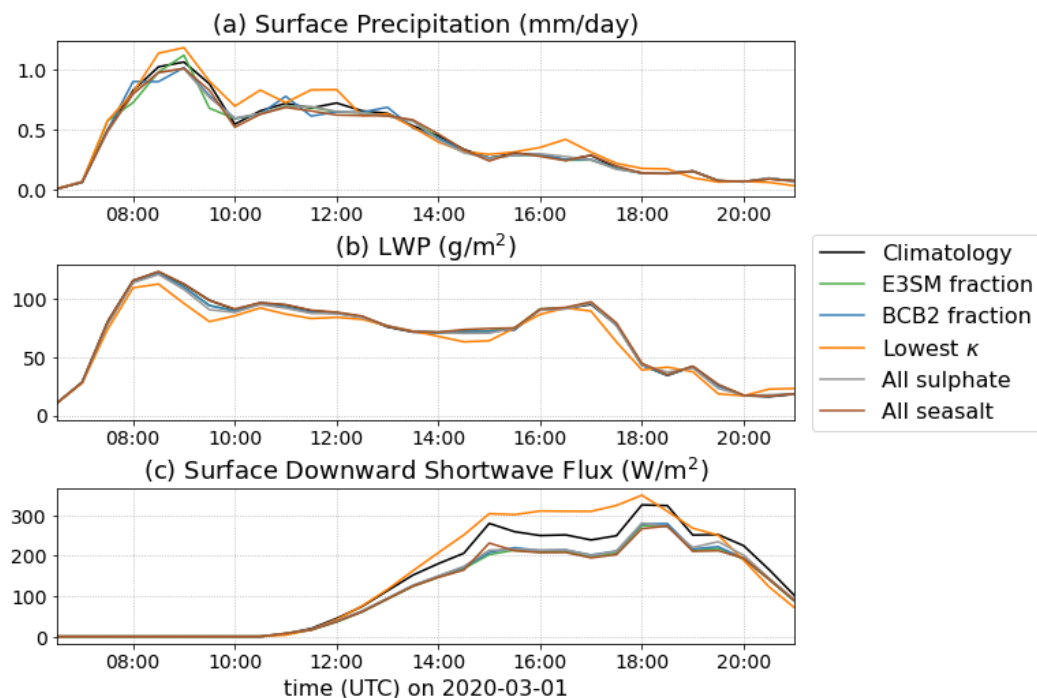
*: κ is calculated from the accumulation mode.

451 The different aerosol hygroscopicity results in different CCN number concentrations (Fig. 12a-13a and 13b+2b13b). As SS
 452 increases, the critical diameter determining CCN number concentration decreases and becomes less sensitive to
 453 hygroscopicity. Therefore, except for the “Lowest κ ” sensitivity run in which the CCN number concentration is almost zero,
 454 the relative difference of CCN number concentration with different aerosol composition settings is smaller for 0.5% SS than
 455 0.1% SS. N_d and R_{eff} are less sensitive to aerosol hygroscopicity ranging from 0.31 to 1.16 compared to CCN number
 456 concentration, and cloud fraction and LWC vary even less. The only outlier is the “Lowest κ ” option with extremely low
 457 hygroscopicity. In this case the extremely low CCN and N_d number concentration (but not zero, as the E3SM model sets a
 458 lower limit of $N_d = 10 \text{ cm}^{-3}$ when a cloud exists) lead to about doubled droplet size (Fig. 13f+2f13f). Therefore, it has a much
 459 stronger surface downward shortwave radiation (Fig. 14c+3e14c). The much larger droplet size also contributes to more
 460 precipitation conversion (Figs. 12g-13g and 14a+3a14a) and depletion of cloud liquid water (Fig. 14b+3b14b). However, the
 461 impact is still very weak and the estimated LWP susceptibility $\frac{d\ln LWP}{d\ln N_d}$ is 0.02 (Fig. 15c+4e15c).



463
464

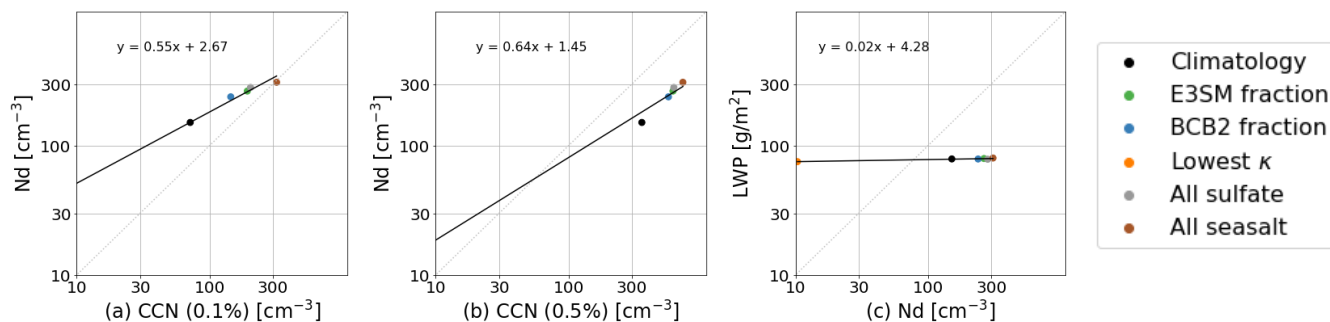
Figure 13: Same as Figure 7 but for E3SM-SCM simulations with different aerosol composition profiles and the same aerosol number concentration (except Climatology) from BCB2 measurements.



465

466

Figure 14: Same as Figure 10 but for E3SM-SCM simulations with different aerosol composition profiles.



467

468

469

Figure 15: Same as Figure 9 but for E3SM-SCM simulations with different aerosol composition profiles. The standard errors of (slope, intercept) for each panel are (0.013, 0.06), (0.024, 0.14), and (0.003, 0.013), respectively.

470

4.3 Sensitivity to aerosol vertical distribution

471

472

473

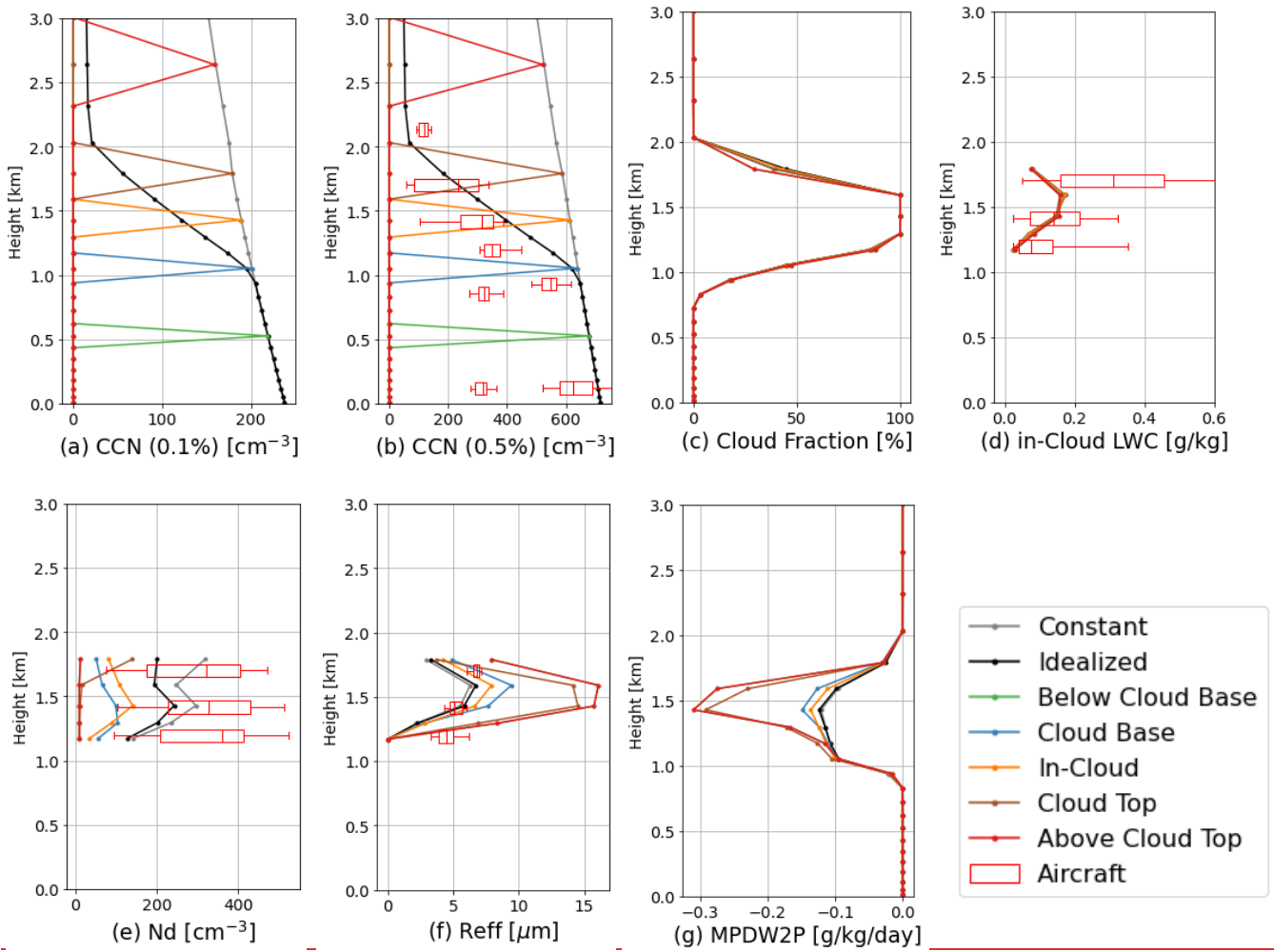
474

475

In many previous modelling studies using observed aerosols, usually only one set of aerosol parameters (i.e., particle number size distribution and composition) was given to the model regardless of the vertical distribution (Liu et al., 2011; Liu et al., 2007; Klein et al., 2009; Lebassi Habtezion and Caldwell, 2015; Li et al., 2023). The observed aerosol information is usually taken from in situ measurements below cloud base (e.g., Liu et al., 2011; Li et al., 2023), assuming that hygroscopic aerosol particles are readily activated into cloud droplets in the saturated air driven by updrafts. However, as aerosol concentration

476 usually decreases with height, the aerosol vertical distribution may be changed by in-cloud scavenging, horizontal transport
477 and vertical mixing, which further affect the cloud microphysical properties (e.g., Lin et al., 2023; Zhang et al., 2021;
478 Kirschler et al., 2022). Indeed, the secondary activation of aerosols above cloud base has been shown to have a significant
479 impact on aerosol convective removal and vertical transport (Wang et al., 2013; Wang et al., 2020). Here we perform a
480 sensitivity study to investigate the impact of aerosols at different vertical levels on E3SM-SCM simulated clouds, and further
481 assess the impact of aerosol vertical distribution on clouds, comparing to results from the simulations with constant vertical
482 aerosol concentration.

483
484 In this set of sensitivity tests, we prescribe aerosols from BCB2 flight leg only for a single model layer, with all other layers
485 being aerosol free. We also perform a simulation with idealized aerosol vertical distribution, where aerosol number
486 concentration decreases linearly from 1 km to 2 km AGL (approximately within the cloud layer) to 10% of its boundary-
487 layer value. Figure 15 shows the vertical profiles of the simulation results. With a prescribed aerosol configuration, the cloud
488 activation process only takes the aerosol information in that layer. However, when aerosol particles are activated into cloud
489 droplets, they are redistributed vertically via vertical transport and sedimentation. The aerosols below cloud base and above
490 cloud top do not participate in the cloud activation process, with $N_d = 10 \text{ cm}^{-3}$ (the low cut-off value) and large R_{eff} similar to
491 the “Lowest κ ” results in Fig. 12. Aerosols within the “Cloud Base” and “In Cloud” layers contribute to about 30% to 40%
492 of N_d activated in the “Constant” aerosol run throughout the simulated cloud layer. The “Cloud Top” aerosols mainly
493 contribute to N_d at the cloud top layer, with a few droplets falling to lower levels causing a reduction in droplet size (Fig.
494 15f). The “Idealized” aerosol profile generally captures the vertical distribution of aircraft measured CCN (Fig. 15b), albeit
495 aircraft measured CCN is overall smaller near the cloud base, likely due to the aerosol scavenging process. Although the
496 decrease of aerosols is 90% at the cloud top, the reduction of N_d in the “Idealized” case is only 20% to 30% less than the
497 “Constant” case (Fig. 15e). Since E3SM-SCM underestimates N_d in this case, it is difficult to demonstrate the value of
498 adding aerosol vertical variation. Moreover, the prescribed aerosol setting in E3SM-SCM limits its ability to study ACI. An
499 interactive aerosol configuration with vertical transport and other processes such as dry and wet deposition enabled is needed
500 to further understand the impact of aerosol vertical distribution on clouds and ACI.



501
 502 **Figure 15:** Same as Figure 7 but for E3SM-SCM simulations with (gray): constant aerosol number concentration (per kg air),
 503 (black): idealized aerosol profile with number concentration decreasing from 1 to 2 km AGL to 10% of the MBL concentration,
 504 and (colours): aerosols in a single layer only. Aircraft measured CCN number concentrations for SS between 0.45% and 0.55%
 505 are overlaid in (b). Aerosol number concentration is from aircraft measurements in the BCB2 leg while aerosol composition is
 506 from E3SM climatology at the BCB2 leg height.

507 **5 Further investigations on of LWP susceptibility**

508 The previous section shows a weakly linear $\frac{d\ln LWP}{d\ln N_d}$ relation in the E3SM-SCM simulations associated with aerosol-induced
 509 precipitation suppression process. This relation is different from from with the non-linear $\frac{d\ln LWP}{d\ln N_d}$ relations seen in the long-
 510 term E3SM GCM simulationssimulationsrun and observations (Tang et al., 2023). In this section, we further investigate the
 511 LWP susceptibility and the related precipitation processes in with more other timesteps of the more SCM simulations.
 512

Since some sensitivity teststestsstudies conducted in Sect. 4 produce similar N_d values (Figs. 10c and 15c), we re-design newathea sensitivity testtest with prescribed aerosols from aircraft measurements at BCB2 leg and perturb the observed aerosol number concentration (N_a) by 0.125, 0.25, 0.5, 2, 4, 8 times for SCM, to examine the susceptibility of LWP and surface precipitation due to N_a perturbations. We also increaseincreaseenhanced the value of a parameter (known as aggregation enhancement factor) in the SCM by aathe factor of 10 to arbitrarily enhance the precipitation suppression effect. The timeseries of surface precipitation and LWP are shown in Fig. 16. With a higher N_a - N_a aerosol number concentration, surface precipitation is more suppressed, leading totowith more LWP remainingremainingeds in the cloud. This effect is more obvious in the first fewseveralfew hours of the simulations. After ~13:00 UTC, the differences of surface precipitation and LWP induceddue toinduced by the perturbation of N_a become muchmoremuch less distinguishabledifficult to visualizedistinguishable, which is consistent with the very weak $\frac{d\ln LWP}{d\ln N_d}$ relation seen at 15:00 – 16:00 UTC in Sect. 4. We hypothesize that dynamical forcing and thermodynamical factors dominatesdominate the LWP budget and cloud evolution during this cold air outbreak event and, therefore, the LWP adjustments due to aerosol perturbations become negligible. Further studies with more cases and associated statistical analyses are needed to verifyassessverify this hypothesis.

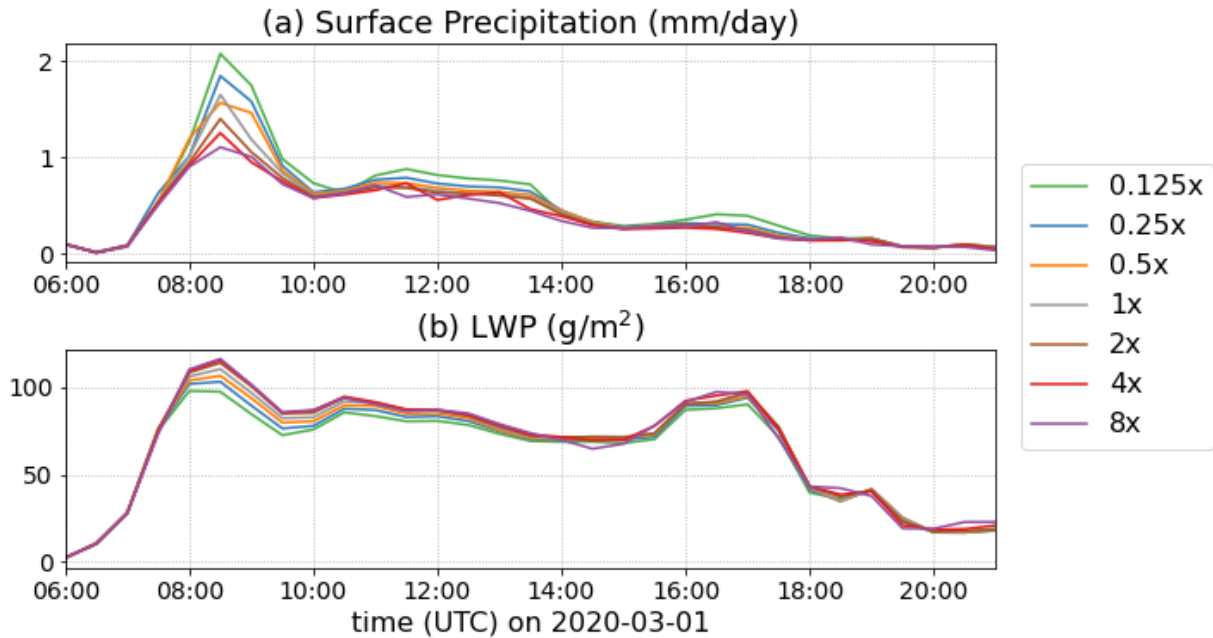
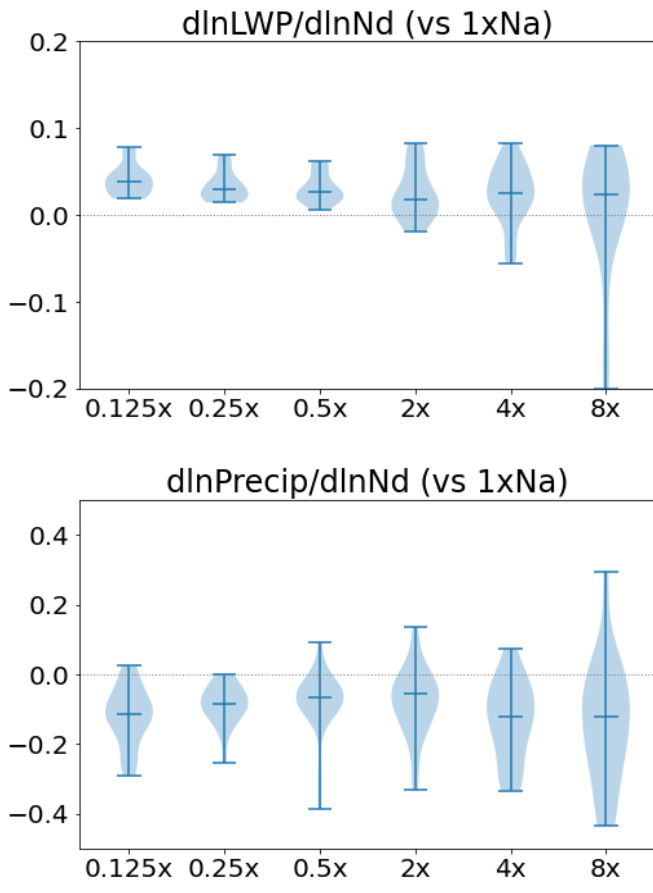


Figure 16: Time series of (a) surface precipitation, and (b) LWP from E3SM-SCM simulations with different aerosol (N_a) aerosol perturbations to N_a -observed below cloud base during the CAO case.

The LWP susceptibility $\frac{d\ln LWP}{d\ln N_d}$, which is now calculated by comparing the perturbed- N_a run and $1xN_a$ SCM simulations at each timestep (1800 s) between 08:00 and 18:00 UTC, is shown in Fig. 17. Also shown is the susceptibility of surface precipitation $\frac{d\ln Precip}{d\ln N_d}$. All the N_a N_a -perturbation tests show a clear positive $\frac{d\ln LWP}{d\ln N_d}$ relation and a negative $\frac{d\ln Precip}{d\ln N_d}$ relation.

533 ~~demonstrating~~ ~~indicating~~ ~~ademonstrating~~ the precipitation suppression effect of aerosols in E3SM-SCM. The spread
 534 in LWP and precipitation susceptibility becomes wider for higher N_a perturbations of higher N_a , indicating that the
 535 precipitation suppression effect becomes ~~more less clear~~ more uncertain with increasing N_a , as ~~N_a the scenario of more~~
 536 ~~aerosols, thus~~ cloud droplets become smaller and less likely to convert into precipitation. The mean of the median $\frac{d\ln LWP}{d\ln N_a}$
 537 values is 0.03, ~~close~~ ~~similar~~ to the slopes estimated in Sect. 4. Again, this weak LWP susceptibility relation is likely due
 538 to the strong dynamical ~~and thermodynamical~~ control for this ~~specific~~ ~~specific~~ CAO case. Long-term SCM simulations with
 539 more cases are needed to further ~~verify~~ ~~assess~~ this hypothesis.



540
 541 **Figure 17: Violin plots of $\frac{d\ln LWP}{d\ln N_a}$ and $\frac{d\ln Precip}{d\ln N_a}$ between 08:00 and 18:00 UTC for the different SCM simulations with perturbed N_a**
 542 **in contrast to the default $1xN_a$. In the violin plots, the horizontal bars represent the upper bound, median value, and the lower**
 543 **bound of the data, while the shading represents the probability density of the data at the corresponding values.**

544 **6 Summary and Discussion**

545 Current [Earth System Models](#) (ESMs) remain largely uncertain in simulating MBL clouds, and [aerosol-cloud interactions](#) (ACI)
 546 related to MBL clouds have been underexplored over the WNAO. With the recent ACTIVATE field campaign conducted

547 over WNAO collecting in-situ and remote-sensing measurements using dual aircraft flying simultaneously, we ~~conduct a~~
548 ~~SCM simulations~~ focusing on a selected CAO case, evaluate the results ~~against~~ ~~with~~ ~~against~~ field observations, and
549 ~~intercompare results with CRM/LES models.~~ Furthermore, we perform several sets of SCM sensitivity
550 ~~experiments~~ ~~studies~~ ~~experiments~~ ~~perform a model intercomparison and sensitivity study for a selected CAO case to~~
551 understand the complex aerosol-cloud interactions related to MBL clouds over WNAO. ~~This comprehensive case study with~~
552 ~~a comprehensive set of aerosol sensitivity simulations provides insight into further designing and investigation of long-term~~
553 ~~SCM simulations for~~ ~~and~~ ~~statistical analysis, which is currently under~~ ~~consideration for a future study~~ ~~study~~ ~~planning.~~

554
555 A unique feature of this study is the multi-scale model intercomparison using SCM, CRM, and LES models, which provides
556 a comprehensive process-level understanding of ACI in more ~~detail~~ ~~details~~ compared to individual models. We conducted
557 E3SMv2 simulations in the SCM mode, and compared ~~them~~ with two WRF model configurations at LES and CRM
558 resolutions, respectively. Overall, the three models all capture the MBL cloud properties, while the E3SM-SCM
559 underestimates cloud droplet number concentration and overestimates droplet size. This is partly due to the relatively low
560 concentration of prescribed aerosols from the E3SM climatology compared to ~~field~~ ~~the observations~~ ~~the observation~~ in this
561 case, and partly due to underestimated updrafts that cannot activate enough aerosol particles into cloud droplets. Note that
562 some parameters in E3SMv2 were tuned to improve the overall performance of subtropical stratocumulus clouds (Ma et al.,
563 2022), but turbulence over the WNAO region is weakened ~~comparing~~ ~~compared~~ to the pre-tuning version (close to E3SMv1)
564 even in a long-term GCM run (Brunke et al., 2022). The evaluation of SCM simulations against the ACTIVATE
565 measurements ~~helps~~ ~~helpful for understanding and improving~~ ~~helps~~ ~~understand and can help improve~~ turbulence
566 representation over this region.

567
568 ~~Among the three models, E3SM SCM and WRF LES are driven by the same large scale and surface forcings derived from~~
569 ~~ERA5 reanalysis, while the WRF CRM model is run as a regional model with nested domains. However, only the WRF~~
570 ~~CRM reproduces the characteristics of cloud rolls in this cold air outbreak case (Chen et al., 2022). With the same large~~
571 ~~scale and surface forcings from WRF CRM, which has weaker subsidence and stronger low level cold and dry air advectons~~
572 ~~than ERA5 forcings, the E3SM SCM and WRF LES produce much thicker clouds than WRF CRM. This indicates that a~~
573 ~~proper match of large scale dynamics, sub-grid scale parameterization, and model configurations is needed to obtain optimal~~
574 ~~model performance.~~

575
576 Several sets of sensitivity experiments are conducted to examine ACI by changing the prescribed aerosol number size
577 distribution and aerosol composition in E3SM-SCM. Aircraft measurements at different heights are used to provide
578 constraints of the aerosol perturbation. Changing aerosol number size distributions dramatically alters the CCN number
579 concentration, thus largely ~~impacting~~ ~~impacting~~ cloud droplet number concentration and size, further influencing the cloud
580 radiative effect. However, changing aerosol composition only shows dramatic impacts in the extremely low hygroscopicity

581 (κ) setting, where ~~there are~~ only very few aerosols ~~being are~~ activated into very large cloud droplets. Changing the overall κ
582 from 0.31 to 1.16 has a smaller impact on cloud microphysical properties. ~~Worth noting, the~~ impact of aerosol
583 composition ~~to on~~ CCN concentration and cloud microphysics can be larger than ~~that~~ shown here as it may also change the
584 aerosol size distribution (Shrivastava et al., 2017).

585
586 In contrast to the clear Twomey effect, the cloud fraction and water content are barely impacted by aerosol perturbations,
587 with a very weak $\frac{d\ln LWP}{d\ln N_d}$ susceptibility of 0.02 ~~during the time of aircraft measurements and 0.03 for the entire simulation~~
588 ~~period~~. The slight positive LWP adjustment is most likely due to the rain suppression effect (Albrecht, 1989). ~~for smaller~~
589 ~~cloud droplets~~. This contradicts the non-linear V-shape $\frac{d\ln LWP}{d\ln N_d}$ curve shown in the long-term E3SM GCM run over the
590 Eastern North Atlantic Ocean (Tang et al., 2023; Varble et al., 2023). Whether this weak positive LWP susceptibility is a
591 case-specific or ~~cloud location cloud regime~~-specific feature and whether SCM can reveal the same cloud susceptibility as
592 ~~the full~~ GCM ~~does require~~ are subject to further study.

593
594 We also performed ~~a sensitivity tests studies tests~~ to ~~test examine~~ the impact of ~~large-scale forcing data and~~ aerosol vertical
595 distribution on cloud simulations. ~~Among the three models for for of intercomparison, E3SM-SCM and WRF-LES are driven~~
596 ~~by the same large-scale and surface forcings derived from ERA5 reanalysis, while the WRF-CRM model is run as a regional~~
597 ~~model with nested domains. domains. However, only the WRF CRM reproduces the characteristics of cloud rolls in this~~
598 ~~old air outbreak case (Chen et al., 2022).~~ With the same large-scale and surface forcings from ~~the~~ WRF-CRM, which has
599 ~~weaker subsidence and stronger low-level cold and dry air advectons than the ERA5 forcings, the E3SM-SCM and WRF-~~
600 ~~LES produce much thicker clouds than WRF-CRM (Figs. S2-S4).~~ This indicates that a proper match of large-scale dynamics,
601 ~~sub-grid scale parameterization, and model configurations is needed to obtain optimal model performance.~~

602
603 ~~In the current SCM framework using observed aerosols, usually only one set of values for aerosol parameters, characterizing~~
604 ~~the spatially mean properties (i.e., particle number size distribution and composition); is fed into the model regardless of the~~
605 ~~aerosol vertical distribution (Liu et al., 2011; Liu et al., 2007; Klein et al., 2009; Lebassi-Habtezion and Caldwell, 2015; Li~~
606 ~~et al., 2023). The prescribed aerosol information based on observations is usually taken from in-situ measurements below the~~
607 ~~cloud base (e.g., Liu et al., 2011; Li et al., 2023), assuming that hygroscopic aerosol particles are readily activated into cloud~~
608 ~~droplets in the saturated air driven by updrafts. However, as aerosol concentration usually decreases with height in the lower~~
609 ~~atmosphere, regional aerosol vertical distribution may be changed by in-cloud scavenging, horizontal transport, and vertical~~
610 ~~mixing, which can further affect cloud microphysical properties by secondary activation above cloud base (Wang et al., 2013;~~
611 ~~Wang et al., 2020). We conducted a sensitivity experiment with a specified aerosol vertical distribution (Fig. S5), but the~~
612 ~~configuration of prescribed aerosols in SCM only shows the response of clouds to aerosols given at the level of cloud~~
613 ~~formation. A more comprehensive consideration of complete aerosol processes (e.g., vertical transport, scavenging,~~

614 ~~deposition, etc.) is needed (e.g., using WRF-CRM or E3SM) to include the cloud and dynamical feedback on aerosols and~~
615 ~~better understand the aerosol-cloud interactions.~~

616 ~~Due to the prescribed aerosol configuration in E3SM SCM, only aerosols at cloud levels can be activated. Adding aerosol~~
617 ~~vertical variation (i.e., decreasing concentration with height) reduces the simulated N_d as there are lower concentrations of~~
618 ~~aerosols in cloudy layers than below cloud base. However, this may not be necessarily better than vertically constant~~
619 ~~aerosols obtained below cloud base, because there is no treatment of vertical transport of aerosols in the SCM configuration.~~
620 ~~A more comprehensive SCM simulation with complete vertical transport and other aerosol processes is needed to better~~
621 ~~simulate ACI and connect field measurements and process-level models with global models.~~

622 **Data Availability**

623 The ACTIVATE aircraft data and GOES-16 satellite data are available from the NASA ACTIVATE project website
624 (<https://asdc.larc.nasa.gov/project/ACTIVATE>, DOI: 10.5067/SUBORBITAL/ACTIVATE/DATA001). ERA5 reanalysis
625 data are available from the Copernicus Climate Change Service Climate Data Store (CDS) (Hersbach et al., 2023a, b).

626 **Code Availability**

627 The E3SMv2 model is available from the U.S. Department of Energy at <https://doi.org/10.11578/E3SM/dc.20210927.1> and
628 the SCM scripts are revised from the E3SM SCM library (<https://github.com/E3SM-Project/scmlib>). The WRF community
629 model is publicly available ~~from the National Center for Atmospheric Research (NCAR) at~~
630 ~~<http://www2.mmm.ucar.edu/wrf/users/> on [wrf](https://code.arm.gov/lasso/lasso-
631 <a href=).~~

632 **Author contribution**

633 ST and HW designed the conceptional ideas. AS, HW, and XZ performed the mission planning and supervision. EC, KT, LZ,
634 and CV participated in mission operation and data curation. ST conducted the SCM simulations, XYL conducted the WRF-
635 LES simulations, and JC conducted the WRF-CRM simulations. ST performed the analysis and prepared the original
636 manuscript. All co-authors contributed to the reviewing and editing of the manuscript.

637 **Competing interests**

638 AS and HW are members of the editorial board of Atmospheric Chemistry and Physics. Other authors declare that they have
639 no conflict of interest.

640 Acknowledgments

641 [We thank two anonymous reviewers for constructive and insightful comments and suggestions.](#) This work was supported
642 through the ACTIVATE Earth Venture Suborbital-3 (EVS-3) investigation, which is funded by NASA's Earth Science
643 Division and managed through the Earth System Science Pathfinder Program Office. The Pacific Northwest National
644 Laboratory (PNNL) is operated for the U.S. Department of Energy by Battelle Memorial Institute under Contract DE-AC05-
645 76RLO1830. The simulations were performed using resources available through Research Computing at PNNL. [The](#)
646 University of Arizona investigators were funded by NASA grant no. 80NSSC19K0442. CV was funded by the German
647 Research Foundation DFG within projects SPP-1294 HALO under Vo1504/7-1 and Vo1504/9-1.

648 References

- 649 Albrecht, B. A.: Aerosols, Cloud Microphysics, and Fractional Cloudiness, *Science*, 245, 1227-1230,
650 <https://doi.org/10.1126/science.245.4923.1227>, 1989.
- 651 Battaglia, A., Kollias, P., Dhillon, R., Roy, R., Tanelli, S., Lamer, K., Grecu, M., Lebsock, M., Watters, D., Mroz, K.,
652 Heymsfield, G., Li, L., and Furukawa, K.: Spaceborne Cloud and Precipitation Radars: Status, Challenges, and Ways
653 Forward, *Reviews of Geophysics*, 58, e2019RG000686, <https://doi.org/10.1029/2019RG000686>, 2020.
- 654 Bock, L., Lauer, A., Schlund, M., Barreiro, M., Bellouin, N., Jones, C., Meehl, G. A., Predoi, V., Roberts, M. J., and Eyring,
655 V.: Quantifying Progress Across Different CMIP Phases With the ESMValTool, *Journal of Geophysical Research:*
656 *Atmospheres*, 125, e2019JD032321, <https://doi.org/10.1029/2019JD032321>, 2020.
- 657 Bogenschütz, P. A., Tang, S., Caldwell, P. M., Xie, S., Lin, W., and Chen, Y. S.: The E3SM version 1 single-column model,
658 *Geosci. Model Dev.*, 13, 4443-4458, <https://doi.org/10.5194/gmd-13-4443-2020>, 2020.
- 659 Bony, S. and Dufresne, J.-L.: Marine boundary layer clouds at the heart of tropical cloud feedback uncertainties in climate
660 models, *Geophysical Research Letters*, 32, <https://doi.org/10.1029/2005GL023851>, 2005.
- 661 Brunke, M. A., Ma, P.-L., Reeves Eyre, J. E. J., Rasch, P. J., Sorooshian, A., and Zeng, X.: Subtropical Marine Low
662 Stratiform Cloud Deck Spatial Errors in the E3SMv1 Atmosphere Model, *Geophysical Research Letters*, 46, 12598-12607,
663 <https://doi.org/10.1029/2019GL084747>, 2019.
- 664 Brunke, M. A., Cutler, L., Urzua, R. D., Corral, A. F., Crosbie, E., Hair, J., Hostetler, C., Kirschler, S., Larson, V., Li, X.-Y.,
665 Ma, P.-L., Minke, A., Moore, R., Robinson, C. E., Scarino, A. J., Schlosser, J., Shook, M., Sorooshian, A., Lee Thornhill, K.,
666 Voigt, C., Wan, H., Wang, H., Winstead, E., Zeng, X., Zhang, S., and Ziemba, L. D.: Aircraft Observations of Turbulence in
667 Cloudy and Cloud-Free Boundary Layers Over the Western North Atlantic Ocean From ACTIVATE and Implications for
668 the Earth System Model Evaluation and Development, *Journal of Geophysical Research: Atmospheres*, 127, e2022JD036480,
669 <https://doi.org/10.1029/2022JD036480>, 2022.
- 670 Chen, J., Liu, Y., Zhang, M., and Peng, Y.: New understanding and quantification of the regime dependence of aerosol-cloud
671 interaction for studying aerosol indirect effects, *Geophysical Research Letters*, 43, 1780-1787,
672 <https://doi.org/10.1002/2016GL067683>, 2016.
- 673 Chen, J., Wang, H., Li, X., Painemal, D., Sorooshian, A., Thornhill, K. L., Robinson, C., and Shingler, T.: Impact of
674 Meteorological Factors on the Mesoscale Morphology of Cloud Streets during a Cold-Air Outbreak over the Western North
675 Atlantic, *Journal of the Atmospheric Sciences*, 79, 2863-2879, <https://doi.org/10.1175/JAS-D-22-0034.1>, 2022.
- 676 Corral, A. F., Braun, R. A., Cairns, B., Gorooh, V. A., Liu, H., Ma, L., Mardi, A. H., Painemal, D., Stamnes, S., van
677 Diedenhoven, B., Wang, H., Yang, Y., Zhang, B., and Sorooshian, A.: An Overview of Atmospheric Features Over the
678 Western North Atlantic Ocean and North American East Coast – Part 1: Analysis of Aerosols, Gases, and Wet Deposition
679 Chemistry, *Journal of Geophysical Research: Atmospheres*, 126, e2020JD032592, <https://doi.org/10.1029/2020JD032592>,
680 2021.
- 681 Dadashazar, H., Corral, A. F., Crosbie, E., Dmitrovic, S., Kirschler, S., McCauley, K., Moore, R., Robinson, C., Schlosser, J.
682 S., Shook, M., Thornhill, K. L., Voigt, C., Winstead, E., Ziemba, L., and Sorooshian, A.: Organic enrichment in droplet

683 residual particles relative to out of cloud over the northwestern Atlantic: analysis of airborne ACTIVATE data, *Atmos.*
684 *Chem. Phys.*, 22, 13897-13913, <https://doi.org/10.5194/acp-22-13897-2022>, 2022a.

685 Dadashazar, H., Crosbie, E., Choi, Y., Corral, A. F., DiGangi, J. P., Diskin, G. S., Dmitrovic, S., Kirschler, S., McCauley, K.,
686 Moore, R. H., Nowak, J. B., Robinson, C. E., Schlosser, J., Shook, M., Thornhill, K. L., Voigt, C., Winstead, E. L., Ziemba,
687 L. D., and Sorooshian, A.: Analysis of MONARC and ACTIVATE Airborne Aerosol Data for Aerosol-Cloud Interaction
688 Investigations: Efficacy of Stairstepping Flight Legs for Airborne In Situ Sampling, *Atmosphere*, 13, 1242,
689 <https://doi.org/10.3390/atmos13081242>, 2022b.

690 Gettelman, A. and Morrison, H.: Advanced Two-Moment Bulk Microphysics for Global Models. Part I: Off-Line Tests and
691 Comparison with Other Schemes, *Journal of Climate*, 28, 1268-1287, <https://doi.org/10.1175/jcli-d-14-00102.1>, 2015.

692 Gettelman, A., Bardeen, C. G., McCluskey, C. S., Järvinen, E., Stith, J., Bretherton, C., McFarquhar, G., Twohy, C.,
693 D'Alessandro, J., and Wu, W.: Simulating Observations of Southern Ocean Clouds and Implications for Climate, *J. Geophys.*
694 *Res. Atmos.*, 125, e2020JD032619, <https://doi.org/10.1029/2020JD032619>, 2020.

695 Golaz, J.-C., Larson, V. E., and Cotton, W. R.: A PDF-Based Model for Boundary Layer Clouds. Part I: Method and Model
696 Description, *J. Atmos. Sci.*, 59, 3540-3551, [https://doi.org/10.1175/1520-0469\(2002\)059<3540:apbmf>2.0.co;2](https://doi.org/10.1175/1520-0469(2002)059<3540:apbmf>2.0.co;2), 2002.

697 Golaz, J.-C., Van Roekel, L. P., Zheng, X., Roberts, A. F., Wolfe, J. D., Lin, W., Bradley, A. M., Tang, Q., Maltrud, M. E.,
698 Forsyth, R. M., Zhang, C., Zhou, T., Zhang, K., Zender, C. S., Wu, M., Wang, H., Turner, A. K., Singh, B., Richter, J. H.,
699 Qin, Y., Petersen, M. R., Mamejtanov, A., Ma, P.-L., Larson, V. E., Krishna, J., Keen, N. D., Jeffery, N., Hunke, E. C.,
700 Hannah, W. M., Guba, O., Griffin, B. M., Feng, Y., Engwirda, D., Di Vittorio, A. V., Dang, C., Conlon, L. M., Chen, C.-C.-
701 J., Brunke, M. A., Bisht, G., Benedict, J. J., Asay-Davis, X. S., Zhang, Y., Zhang, M., Zeng, X., Xie, S., Wolfram, P. J., Vo,
702 T., Veneziani, M., Tesfa, T. K., Sreepathi, S., Salinger, A. G., Jack Reeves Eyre, J. E., Prather, M. J., Mahajan, S., Li, Q.,
703 Jones, P. W., Jacob, R. L., Huebler, G. W., Huang, X., Hillman, B. R., Harrop, B. E., Foucar, J. G., Fang, Y., Comeau, D. S.,
704 Caldwell, P. M., Bartoletti, T., Balaguru, K., Taylor, M. A., McCoy, R. B., Leung, L. R., and Bader, D. C.: The DOE E3SM
705 Model Version 2: Overview of the physical model and initial model evaluation, *Journal of Advances in Modeling Earth*
706 *Systems*, n/a, e2022MS003156, <https://doi.org/10.1029/2022MS003156>, 2022.

707 Hartmann, D. L., Ockert-Bell, M. E., and Michelsen, M. L.: The Effect of Cloud Type on Earth's Energy Balance: Global
708 Analysis, *Journal of Climate*, 5, 1281-1304, [https://doi.org/10.1175/1520-0442\(1992\)005<1281:TEOCTO>2.0.CO;2](https://doi.org/10.1175/1520-0442(1992)005<1281:TEOCTO>2.0.CO;2), 1992.

709 Hersbach, H., Bell, B., Berrisford, P., Biavati, G., Horányi, A., Muñoz Sabater, J., Nicolas, J., Peubey, C., Radu, R., Rozum,
710 I., Schepers, D., Simmons, A., Soci, C., Dee, D., and Thépaut, J.-N.: ERA5 hourly data on pressure levels from 1940 to
711 present, Copernicus Climate Change Service (C3S) Climate Data Store (CDS) [dataset],
712 <https://doi.org/10.24381/cds.bd0915c6>, 2023a. Accessed 02-March-2023.

713 Hersbach, H., Bell, B., Berrisford, P., Biavati, G., Horányi, A., Muñoz Sabater, J., Nicolas, J., Peubey, C., Radu, R., Rozum,
714 I., Schepers, D., Simmons, A., Soci, C., Dee, D., and Thépaut, J.-N.: ERA5 hourly data on single levels from 1940 to present,
715 Copernicus Climate Change Service (C3S) Climate Data Store (CDS) [dataset], <https://doi.org/10.24381/cds.adbb2d47>,
716 2023b. Accessed 02-March-2023.

717 Hersbach, H., Bell, B., Berrisford, P., Hirahara, S., Horányi, A., Muñoz-Sabater, J., Nicolas, J., Peubey, C., Radu, R.,
718 Schepers, D., Simmons, A., Soci, C., Abdalla, S., Abellan, X., Balsamo, G., Bechtold, P., Biavati, G., Bidlot, J., Bonavita,
719 M., De Chiara, G., Dahlgren, P., Dee, D., Diamantakis, M., Dragani, R., Flemming, J., Forbes, R., Fuentes, M., Geer, A.,
720 Haimberger, L., Healy, S., Hogan, R. J., Hólm, E., Janisková, M., Keeley, S., Laloyaux, P., Lopez, P., Lupu, C., Radnoti, G.,
721 de Rosnay, P., Rozum, I., Vamborg, F., Villaume, S., and Thépaut, J.-N.: The ERA5 global reanalysis, *Quarterly Journal of*
722 *the Royal Meteorological Society*, 146, 1999-2049, <https://doi.org/10.1002/qj.3803>, 2020.

723 IPCC, Stocker, T. F., Qin, D., Plattner, G.-K., Tignor, M., Allen, S. K., Boschung, J., Nauels, A., Xia, Y., Bex, V., and
724 Midgley, P. M. (Eds.): *Climate Change 2013: The Physical Science Basis*. Contribution of Working Group I to the Fifth
725 Assessment Report of the Intergovernmental Panel on Climate Change, Cambridge University Press, Cambridge, United
726 Kingdom and New York, NY, USA, 1535 pp., <https://doi.org/10.1017/CBO9781107415324>, 2013.

727 IPCC: *Climate Change 2021: The Physical Science Basis*. Contribution of Working Group I to the Sixth Assessment Report
728 of the Intergovernmental Panel on Climate Change, Cambridge University Press, Cambridge, United Kingdom and New
729 York, NY, USA, 2391 pp., <https://doi.org/10.1017/9781009157896>, 2021.

730 Kirschler, S., Voigt, C., Anderson, B. E., Chen, G., Crosbie, E. C., Ferrare, R. A., Hahn, V., Hair, J. W., Kaufmann, S.,
731 Moore, R. H., Painemal, D., Robinson, C. E., Sanchez, K. J., Scarino, A. J., Shingler, T. J., Shook, M. A., Thornhill, K. L.,
732 Winstead, E. L., Ziemba, L. D., and Sorooshian, A.: Overview and statistical analysis of boundary layer clouds and

733 precipitation over the western North Atlantic Ocean, *Atmos. Chem. Phys.*, 23, 10731-10750, [https://doi.org/10.5194/acp-23-](https://doi.org/10.5194/acp-23-10731-2023)
734 [10731-2023](https://doi.org/10.5194/acp-23-10731-2023), 2023.

735 Kirschler, S., Voigt, C., Anderson, B., Campos Braga, R., Chen, G., Corral, A. F., Crosbie, E., Dadashazar, H., Ferrare, R. A.,
736 Hahn, V., Hendricks, J., Kaufmann, S., Moore, R., Pöhlker, M. L., Robinson, C., Scarino, A. J., Schollmayer, D., Shook, M.
737 A., Thornhill, K. L., Winstead, E., Ziemba, L. D., and Sorooshian, A.: Seasonal updraft speeds change cloud droplet number
738 concentrations in low-level clouds over the western North Atlantic, *Atmos. Chem. Phys.*, 22, 8299-8319,
739 <https://doi.org/10.5194/acp-22-8299-2022>, 2022.

740 Klein, S. A., McCoy, R. B., Morrison, H., Ackerman, A. S., Avramov, A., Boer, G. d., Chen, M., Cole, J. N. S., Del Genio,
741 A. D., Falk, M., Foster, M. J., Fridlind, A., Golaz, J.-C., Hashino, T., Harrington, J. Y., Hoose, C., Khairoutdinov, M. F.,
742 Larson, V. E., Liu, X., Luo, Y., McFarquhar, G. M., Menon, S., Neggers, R. A. J., Park, S., Poellot, M. R., Schmidt, J. M.,
743 Sednev, I., Shipway, B. J., Shupe, M. D., Spangenberg, D. A., Sud, Y. C., Turner, D. D., Veron, D. E., Salzen, K. v., Walker,
744 G. K., Wang, Z., Wolf, A. B., Xie, S., Xu, K.-M., Yang, F., and Zhang, G.: Intercomparison of model simulations of mixed-
745 phase clouds observed during the ARM Mixed-Phase Arctic Cloud Experiment. I: single-layer cloud, *Q. J. R. Meteorol. Soc.*,
746 135, 979-1002, <https://doi.org/10.1002/qj.416>, 2009.

747 Larson, V. E. and Golaz, J.-C.: Using Probability Density Functions to Derive Consistent Closure Relationships among
748 Higher-Order Moments, *Mon. Weather Rev.*, 133, 1023-1042, <https://doi.org/10.1175/mwr2902.1>, 2005.

749 Lebassi-Habtezion, B. and Caldwell, P. M.: Aerosol specification in single-column Community Atmosphere Model version
750 5, *Geosci. Model Dev.*, 8, 817-828, <https://doi.org/10.5194/gmd-8-817-2015>, 2015.

751 Li, X.-Y., Wang, H., Chen, J., Endo, S., Kirschler, S., Voigt, C., Crosbie, E., Ziemba, L. D., Painemal, D., Cairns, B., Hair, J.
752 W., Corral, A. F., Robinson, C., Dadashazar, H., Sorooshian, A., Chen, G., Ferrare, R. A., Kleb, M. M., Liu, H., Moore, R.,
753 Scarino, A. J., Shook, M. A., Shingler, T. J., Thornhill, K. L., Tornow, F., Xiao, H., and Zeng, X.: Large-Eddy Simulations
754 of Marine Boundary Layer Clouds Associated with Cold-Air Outbreaks during the ACTIVATE Campaign. Part II: Aerosol-
755 Meteorology-Cloud Interaction, *Journal of the Atmospheric Sciences*, 80, 1025-1045, [https://doi.org/10.1175/JAS-D-21-](https://doi.org/10.1175/JAS-D-21-0324.1)
756 [0324.1](https://doi.org/10.1175/JAS-D-21-0324.1), 2023.

757 Li, X.-Y., Wang, H., Chen, J., Endo, S., George, G., Cairns, B., Chellappan, S., Zeng, X., Kirschler, S., Voigt, C.,
758 Sorooshian, A., Crosbie, E., Chen, G., Ferrare, R. A., Gustafson, W. I., Hair, J. W., Kleb, M. M., Liu, H., Moore, R.,
759 Painemal, D., Robinson, C., Scarino, A. J., Shook, M., Shingler, T. J., Thornhill, K. L., Tornow, F., Xiao, H., Ziemba, L. D.,
760 and Zuidema, P.: Large-Eddy Simulations of Marine Boundary Layer Clouds Associated with Cold-Air Outbreaks during
761 the ACTIVATE Campaign. Part I: Case Setup and Sensitivities to Large-Scale Forcings, *Journal of the Atmospheric*
762 *Sciences*, 79, 73-100, <https://doi.org/10.1175/jas-d-21-0123.1>, 2022.

763 Lin, Y., Takano, Y., Gu, Y., Wang, Y., Zhou, S., Zhang, T., Zhu, K., Wang, J., Zhao, B., Chen, G., Zhang, D., Fu, R., and
764 Seinfeld, J.: Characterization of the aerosol vertical distributions and their impacts on warm clouds based on multi-year
765 ARM observations, *Science of The Total Environment*, 904, 166582, <https://doi.org/10.1016/j.scitotenv.2023.166582>, 2023.

766 Liu, X., Xie, S., and Ghan, S. J.: Evaluation of a new mixed-phase cloud microphysics parameterization with CAM3 single-
767 column model and M-PACE observations, *Geophys. Res. Lett.*, 34, n/a-n/a, <https://doi.org/10.1029/2007GL031446>, 2007.

768 Liu, X., Ma, P. L., Wang, H., Tilmes, S., Singh, B., Easter, R. C., Ghan, S. J., and Rasch, P. J.: Description and evaluation of
769 a new four-mode version of the Modal Aerosol Module (MAM4) within version 5.3 of the Community Atmosphere Model,
770 *Geosci. Model Dev.*, 9, 505-522, <https://doi.org/10.5194/gmd-9-505-2016>, 2016.

771 Liu, X., Xie, S., Boyle, J., Klein, S. A., Shi, X., Wang, Z., Lin, W., Ghan, S. J., Earle, M., Liu, P. S. K., and Zelenyuk, A.:
772 Testing cloud microphysics parameterizations in NCAR CAM5 with ISDAC and M-PACE observations, *J. Geophys. Res.*
773 *Atmos.*, 116, <https://doi.org/10.1029/2011jd015889>, 2011.

774 Liu, X., Easter, R. C., Ghan, S. J., Zaveri, R., Rasch, P., Shi, X., Lamarque, J. F., Gettelman, A., Morrison, H., Vitt, F.,
775 Conley, A., Park, S., Neale, R., Hannay, C., Ekman, A. M. L., Hess, P., Mahowald, N., Collins, W., Iacono, M. J.,
776 Bretherton, C. S., Flanner, M. G., and Mitchell, D.: Toward a minimal representation of aerosols in climate models:
777 description and evaluation in the Community Atmosphere Model CAM5, *Geosci. Model Dev.*, 5, 709-739,
778 <https://doi.org/10.5194/gmd-5-709-2012>, 2012.

779 Ma, P. L., Harrop, B. E., Larson, V. E., Neale, R. B., Gettelman, A., Morrison, H., Wang, H., Zhang, K., Klein, S. A.,
780 Zelinka, M. D., Zhang, Y., Qian, Y., Yoon, J. H., Jones, C. R., Huang, M., Tai, S. L., Singh, B., Bogenschutz, P. A., Zheng,
781 X., Lin, W., Quaas, J., Chepfer, H., Brunke, M. A., Zeng, X., Mülmenstädt, J., Hagos, S., Zhang, Z., Song, H., Liu, X.,
782 Pritchard, M. S., Wan, H., Wang, J., Tang, Q., Caldwell, P. M., Fan, J., Berg, L. K., Fast, J. D., Taylor, M. A., Golaz, J. C.,

783 Xie, S., Rasch, P. J., and Leung, L. R.: Better calibration of cloud parameterizations and subgrid effects increases the fidelity
784 of the E3SM Atmosphere Model version 1, *Geosci. Model Dev.*, 15, 2881-2916, <https://doi.org/10.5194/gmd-15-2881-2022>,
785 2022.

786 Minnis, P., Nguyen, L., Palikonda, R., Heck, P. W., Spangenberg, D. A., Doelling, D. R., Ayers, J. K., Smith, J. W. L.,
787 Khaiyer, M. M., Trepte, Q. Z., Avey, L. A., Chang, F.-L., Yost, C. R., Chee, T. L., and Szedung, S.-M.: Near-real time cloud
788 retrievals from operational and research meteorological satellites, *Proc. SPIE Europe Remote Sens.*, Cardiff, Wales, UK., 15-
789 18 September, 710703, <https://doi.org/10.1117/12.800344>, 2008.

790 Minnis, P., Sun-Mack, S., Young, D. F., Heck, P. W., Garber, D. P., Chen, Y., Spangenberg, D. A., Arduini, R. F., Trepte, Q.
791 Z., Smith, W. L., Ayers, J. K., Gibson, S. C., Miller, W. F., Hong, G., Chakrapani, V., Takano, Y., Liou, K. N., Xie, Y., and
792 Yang, P.: CERES Edition-2 Cloud Property Retrievals Using TRMM VIRS and Terra and Aqua MODIS Data—Part I:
793 Algorithms, *IEEE Transactions on Geoscience and Remote Sensing*, 49, 4374-4400,
794 <https://doi.org/10.1109/TGRS.2011.2144601>, 2011.

795 Painemal, D., Corral, A. F., Sorooshian, A., Brunke, M. A., Chellappan, S., Afzali Goroooh, V., Ham, S.-H., O'Neill, L.,
796 Smith Jr., W. L., Tselioudis, G., Wang, H., Zeng, X., and Zuidema, P.: An Overview of Atmospheric Features Over the
797 Western North Atlantic Ocean and North American East Coast—Part 2: Circulation, Boundary Layer, and Clouds, *Journal of*
798 *Geophysical Research: Atmospheres*, 126, e2020JD033423, <https://doi.org/10.1029/2020JD033423>, 2021.

799 Randall, D. A., Xu, K.-M., Somerville, R. J. C., and Iacobellis, S.: Single-Column Models and Cloud Ensemble Models as
800 Links between Observations and Climate Models, *J. Climate*, 9, 1683-1697, [https://doi.org/10.1175/1520-
801 0442\(1996\)009<1683:SCMACE>2.0.CO;2](https://doi.org/10.1175/1520-0442(1996)009<1683:SCMACE>2.0.CO;2), 1996.

802 Seethala, C., Zuidema, P., Edson, J., Brunke, M., Chen, G., Li, X. Y., Painemal, D., Robinson, C., Shingler, T., Shook, M.,
803 Sorooshian, A., Thornhill, L., Tornow, F., Wang, H., Zeng, X., and Ziemba, L.: On Assessing ERA5 and MERRA2
804 Representations of Cold-Air Outbreaks Across the Gulf Stream, *Geophys Res Lett*, 48,
805 <https://doi.org/10.1029/2021gl094364>, 2021.

806 Shrivastava, M., Cappa, C. D., Fan, J., Goldstein, A. H., Guenther, A. B., Jimenez, J. L., Kuang, C., Laskin, A., Martin, S. T.,
807 Ng, N. L., Petaja, T., Pierce, J. R., Rasch, P. J., Roldin, P., Seinfeld, J. H., Shilling, J., Smith, J. N., Thornton, J. A.,
808 Volkamer, R., Wang, J., Worsnop, D. R., Zaveri, R. A., Zelenyuk, A., and Zhang, Q.: Recent advances in understanding
809 secondary organic aerosol: Implications for global climate forcing, *Reviews of Geophysics*, 55, 509-559,
810 <https://doi.org/10.1002/2016RG000540>, 2017.

811 Sorooshian, A., Corral, A. F., Braun, R. A., Cairns, B., Crosbie, E., Ferrare, R., Hair, J., Kleb, M. M., Hossein Mardi, A.,
812 Maring, H., McComiskey, A., Moore, R., Painemal, D., Scarino, A. J., Schlosser, J., Shingler, T., Shook, M., Wang, H.,
813 Zeng, X., Ziemba, L., and Zuidema, P.: Atmospheric Research Over the Western North Atlantic Ocean Region and North
814 American East Coast: A Review of Past Work and Challenges Ahead, *J. Geophys. Res. Atmos.*, 125, e2019JD031626,
815 <https://doi.org/10.1029/2019JD031626>, 2020.

816 Sorooshian, A., Anderson, B., Bauer, S. E., Braun, R. A., Cairns, B., Crosbie, E., Dadashazar, H., Diskin, G., Ferrare, R.,
817 Flagan, R. C., Hair, J., Hostetler, C., Jonsson, H. H., Kleb, M. M., Liu, H., MacDonald, A. B., McComiskey, A., Moore, R.,
818 Painemal, D., Russell, L. M., Seinfeld, J. H., Shook, M., Smith, W. L., Thornhill, K., Tselioudis, G., Wang, H., Zeng, X.,
819 Zhang, B., Ziemba, L., and Zuidema, P.: Aerosol–Cloud–Meteorology Interaction Airborne Field Investigations: Using
820 Lessons Learned from the U.S. West Coast in the Design of ACTIVATE off the U.S. East Coast, *Bulletin of the American*
821 *Meteorological Society*, 100, 1511-1528, <https://doi.org/10.1175/BAMS-D-18-0100.1>, 2019.

822 Sorooshian, A., Alexandrov, M. D., Bell, A. D., Bennett, R., Betito, G., Burton, S. P., Buzanowicz, M. E., Cairns, B.,
823 Chemyakin, E. V., Chen, G., Choi, Y., Collister, B. L., Cook, A. L., Corral, A. F., Crosbie, E. C., van Dierenhoven, B.,
824 DiGangi, J. P., Diskin, G. S., Dmitrovic, S., Edwards, E.-L., Fenn, M. A., Ferrare, R. A., van Gilst, D., Hair, J. W., Harper, D.
825 B., Hilario, M. R. A., Hostetler, C. A., Jester, N., Jones, M., Kirschler, S., Kleb, M. M., Kusterer, J. M., Leavor, S., Lee, J.
826 W., Liu, H., McCauley, K., Moore, R. H., Nied, J., Notari, A., Nowak, J. B., Painemal, D., Phillips, K. E., Robinson, C. E.,
827 Scarino, A. J., Schlosser, J. S., Seaman, S. T., Seethala, C., Shingler, T. J., Shook, M. A., Sinclair, K. A., Smith Jr, W. L.,
828 Spangenberg, D. A., Starnes, S. A., Thornhill, K. L., Voigt, C., Vömel, H., Wasilewski, A. P., Wang, H., Winstead, E. L.,
829 Zeider, K., Zeng, X., Zhang, B., Ziemba, L. D., and Zuidema, P.: Spatially coordinated airborne data and complementary
830 products for aerosol, gas, cloud, and meteorological studies: the NASA ACTIVATE dataset, *Earth System Science Data*, 15,
831 3419-3472, <https://doi.org/10.5194/essd-15-3419-2023>, 2023.

832 Tang, S., Varble, A. C., Fast, J. D., Zhang, K., Wu, P., Dong, X., Mei, F., Pekour, M., Hardin, J. C., and Ma, P. L.: Earth
833 System Model Aerosol-Cloud Diagnostics Package (ESMAC Diags) Version 2: Assessments of Aerosols, Clouds and
834 Aerosol-Cloud Interactions Through Field Campaign and Long-Term Observations, *Geosci. Model Dev. Discuss.*, 2023, 1-
835 32, <https://doi.org/10.5194/gmd-2023-51>, 2023.

836 Twomey, S.: The nuclei of natural cloud formation part II: The supersaturation in natural clouds and the variation of cloud
837 droplet concentration, *Geofisica pura e applicata*, 43, 243-249, <https://doi.org/10.1007/BF01993560>, 1959.

838 Twomey, S.: The Influence of Pollution on the Shortwave Albedo of Clouds, *J. Atmos. Sci.*, 34, 1149-1152,
839 [https://doi.org/10.1175/1520-0469\(1977\)034<1149:TIOPOT>2.0.CO;2](https://doi.org/10.1175/1520-0469(1977)034<1149:TIOPOT>2.0.CO;2), 1977.

840 Varble, A. C., Ma, P. L., Christensen, M. W., Mülmenstädt, J., Tang, S., and Fast, J.: Evaluation of liquid cloud albedo
841 susceptibility in E3SM using coupled eastern North Atlantic surface and satellite retrievals, *Atmos. Chem. Phys.*, 23, 13523-
842 13553, <https://doi.org/10.5194/acp-23-13523-2023>, 2023.

843 Vömel, H., Sorooshian, A., Robinson, C., Shingler, T. J., Thornhill, K. L., and Ziemba, L. D.: Dropsonde observations
844 during the Aerosol Cloud meTeorology Interactions oVer the western ATlantic Experiment, *Scientific Data*, 10, 753,
845 <https://doi.org/10.1038/s41597-023-02647-5>, 2023.

846 Wang, H., Easter, R. C., Rasch, P. J., Wang, M., Liu, X., Ghan, S. J., Qian, Y., Yoon, J. H., Ma, P. L., and Vinoj, V.:
847 Sensitivity of remote aerosol distributions to representation of cloud-aerosol interactions in a global climate model, *Geosci.*
848 *Model Dev.*, 6, 765-782, <https://doi.org/10.5194/gmd-6-765-2013>, 2013.

849 Wang, H., Easter, R. C., Zhang, R., Ma, P.-L., Singh, B., Zhang, K., Ganguly, D., Rasch, P. J., Burrows, S. M., Ghan, S. J.,
850 Lou, S., Qian, Y., Yang, Y., Feng, Y., Flanner, M., Leung, R. L., Liu, X., Shrivastava, M., Sun, J., Tang, Q., Xie, S., and
851 Yoon, J.-H.: Aerosols in the E3SM Version 1: New Developments and Their Impacts on Radiative Forcing, *J. Adv. Model.*
852 *Earth Syst.*, 12, e2019MS001851, <https://doi.org/10.1029/2019ms001851>, 2020.

853 Warren, S. G., Hahn, C. J., London, J., Chervin, R. M., and Jenne, R. L.: Global distribution of total cloud cover and cloud
854 type amounts over the ocean, US DOE Office of Energy Research, Washington, DC (USA)

855 National Center for Atmospheric Research, Boulder, CO (USA), Technical Report, Report number: DOE/ER-0406, 305 pp,
856 10.2172/5415329, 1988.

857 Wood, R.: Stratocumulus Clouds, *Monthly Weather Review*, 140, 2373-2423, <https://doi.org/10.1175/mwr-d-11-00121.1>,
858 2012.

859 Xie, S., Wang, Y.-C., Lin, W., Ma, H.-Y., Tang, Q., Tang, S., Zheng, X., Golaz, J.-C., Zhang, G. J., and Zhang, M.:
860 Improved Diurnal Cycle of Precipitation in E3SM With a Revised Convective Triggering Function, *J. Adv. Model. Earth*
861 *Syst.*, 11, 2290-2310, <https://doi.org/10.1029/2019ms001702>, 2019.

862 Zhang, G. J. and McFarlane, N. A.: Sensitivity of climate simulations to the parameterization of cumulus convection in the
863 Canadian climate centre general circulation model, *Atmosphere-Ocean*, 33, 407-446,
864 <https://doi.org/10.1080/07055900.1995.9649539>, 1995.

865 Zhang, M., Deng, X., Zhu, R., Ren, Y., and Xue, H.: The Impact of Aerosol Vertical Distribution on a Deep Convective
866 Cloud, *Atmosphere*, 12, 675, <https://doi.org/10.3390/atmos12060675>, 2021.

867